https://doi.org/10.5194/egusphere-2026-3965
Preprint. Discussion started: 28 August 2026
© Author(s) 2026. CC BY 4.0 License.

Application of a Method for Fine-Tuning Differential Reflectivity in an X-Band Phased-Array Weather Radar to a Squall Line

Ling Yang[1,2,3], Jinyan Xu[1,2], Mingliang Xu[4], Pengbo Wu[1,2], Tianyi Chen[1,2], Jia Li[5], Chong Wu[6] and Chao Chen[7]

[1]College of Electronic Engineering, Chengdu University of Information Technology, Chengdu 610225, China
[2]CMA Key Laboratory of Atmospheric Sounding, Chengdu 610225, China
[3]Institute of Low-Altitude Meteorological Intelligence Technology, Chengdu 610225, China
[4]College of Optoelectronic Engineering, Chengdu University of Information Technology, Chengdu 610225, China
[5]HuaYun METSTAR Radar (Beijing) Company, Limited Beijing, 10094, China
[6]Chinese Academy of Meteorological Sciences, Beijing 100081, China
[7]Guangdong Meteorological Observatory, Guangzhou 510640, China

Correspondence to: Jia. Li (jia.li@metstar.net)

Abstract. Maintaining the calibration accuracy of differential reflectivity (Z_{DR}) within 0.2 dB for both X-band and S-band weather radars is a prevailing operational requirement. With the advancement of weather radar detection technologies, X-band phased-array weather radars (XPAR) offer superior spatiotemporal resolution and are particularly advantageous for low-altitude detection. However, they suffer from Z_{DR} bias caused by the deterioration of antenna isolation, which results from the variation of the normal direction along with changes in the beam pointing angle. To systematically investigate the primary factors affecting XPAR data quality, this study selects synchronized observations from XPAR and an S-band polarimetric radar (SPOL) over multiple periods, and proposes a refined Z_{DR} correction algorithm (RC-Z_{DR}) that addresses four aspects: systematic bias correction, attenuation correction, cross-polarization isolation degradation compensation specific to phased-array systems, and correction for anomalous radial interference. For systematic bias, light rain below the zero-degree layer is employed as natural calibration targets, and a weighted correction method (Bias-WZ_{DR}) based on the mean Z_{DR} values at three elevation angles whose beam pointing angles are close to the array normal direction (0°) is proposed to mitigate the interference of cross-polarization isolation on system calibration. Attenuation correction formulas are applied to moderate and heavy precipitation regions. In addition, a 9.4 GHz dual-polarized microstrip antenna array is modeled using High Frequency Structure Simulator (HFSS) electromagnetic simulations to reveal the variations of antenna gain and 3 dB beamwidth with beam pointing angle. Based on this, a quadratic function correction method for cross-polarization isolation (QCCPI) is proposed to quantitatively compensate for the degradation bias between different elevation angles. A composite threshold method is adopted to filter out radial interferences in low-level XPAR observations, further improving the quality of basic data. During a moderate rain event at the ZG100 site, after QCCPI correction, the maximum difference in mean Z_{DR} among different beam pointing angles decreased from 0.45 dB to 0.27 dB. The proposed RC-Z_{DR} method is then applied to a squall line event observed at the ZG100 site on June 6, 2023. Spatiotemporal matching and comparison with SPOL data demonstrate that the corrected Z_{DR} data can more accurately capture the polarimetric signatures of the strong convective core of the squall line. The

https://doi.org/10.5194/egusphere-2026-3965
Preprint. Discussion started: 28 August 2026
© Author(s) 2026. CC BY 4.0 License.

overall mean Z_{DR} of XPAR across all elevation angles is corrected from -0.591 dB to 0.226 dB, and the bias relative to SPOL observations is reduced from 0.619 dB to 0.198 dB. This work provides a scientific and efficient technical support for operational quality control and performance evaluation of next-generation phased-array weather radars.

1 Introduction

Against the backdrop of global climate change and the growing frequency of extreme hazardous weather events, high-spatiotemporal-resolution monitoring of meso- and micro-scale weather systems such as severe convective storms, tornadoes (Zhou et al., 2025), and microbursts has emerged as a core research priority in atmospheric science. Constrained by their mechanical scanning architecture, conventional parabolic-antenna weather radars (e.g., WSR-88D and CINRAD-SA/SB) typically take 4-6 minutes to complete a full volume scan, which makes it difficult to capture the fine-scale features of short-lived, rapidly evolving convective cells (Weber et al., 2007).

Since 2002, when the National Severe Storms Laboratory (NSSL) in the United States retrofitted a decommissioned Navy Aegis (AN/SPY-1) radar for meteorological use, the potential of phased array technology in meteorological observation has been widely demonstrated (Zrnic et al., 2007). To overcome these limitations, Phased Array Weather Radar (PAR) technology has emerged as a leading solution due to its electronic scanning mechanism, which enables near-instantaneous beam steering by controlling the phase of the array elements, thereby significantly enhancing observational efficiency.

Subsequent successful applications of one-dimensional phased-array mobile systems, such as the MWR-05XP, have demonstrated a temporal advantage far surpassing that of conventional radar in capturing tornado vortex features (TVS) (French et al., 2014). Meanwhile, China has also made significant strides in the field of phased array radar, from the development of an S-band proof-of-concept prototype in 2007 (Zhang et al., 2007) to the testing of the X-band Phased Array Radar (XPAR) with multi-beam observation capabilities in 2009 (Liu et al., 2014). In 2017, Japan developed and deployed a dual-polarization phased-array weather radar in the Tokyo Metropolitan Area, capable of full-sky scanning with a resolution of up to 100 m, a scan cycle of 10-30 s, and a coverage radius of 80 km (Ushio et al., 2022); With its recent deployment in disaster prevention and mitigation networks in megacities, phased array technology has become a crucial pillar of short-term weather forecasting in China (Zhang et al., 2023). Among all phased array architectures, the first and only fully digital phased array radar specifically designed for meteorological observations was developed by the Advanced Radar Research Center at the University of Oklahoma. It has been in operation since 2023 and is used to demonstrate the capabilities of fully digital phased array radar in weather observation (Palmer et al., 2025).

However, while offering the advantage of high spatiotemporal resolution, dual-polarization phased-array weather radars still face significant challenges, including insufficient data quality stability, the high complexity of quality control algorithms (Zhou et al., 2022), and the difficulty of calibrating polarization parameters. The Differential Reflectivity Factor (Z_{DR}) is a core polarization parameter characterizing the microphysical properties of water-bearing particles (JieLa et al., 2020). Defined as the ratio of horizontal to vertical polarization reflectivity, its observational accuracy directly determines the reliability of

https://doi.org/10.5194/egusphere-2026-3965
Preprint. Discussion started: 28 August 2026
© Author(s) 2026. CC BY 4.0 License.

precipitation particle phase identification and quantitative precipitation estimation (QPE) results (Bringi et al., 2011; Cifelli et al., 2011; Giangrande and Ryzhkov, 2008; Palmer and Schvartzman, 2025).

As a blind-spot observation device for SPOL radars, X-band phased-array weather radars (XPAR) are typically mounted at a height of approximately 100 m, making them susceptible to ground clutter interference. Combined with factors such as hardware aging and factory calibration deviations, this can introduce systematic errors into Z_{DR} measurements, which is a common issue shared by traditional mechanically scanned S-band and C-band radars. However, unlike traditional radars, phased-array weather radars also face a more pronounced systemic issue: beam characteristics dynamically change with the antenna's beam steering angle. When the beam deviates from the array normal due to electronic scanning, the effective radiated area of the planar phased array decreases, resulting in reduced antenna gain and beamwidth expansion. Simultaneously, the cross-polarization isolation (CPI) between the horizontal and vertical polarization channels deteriorates, ultimately leading to a significant degradation of CPI in the Z_{DR} during three-dimensional detection. Previous studies have shown that in phased array systems, fluctuations in transmit and receive gains during elevation or azimuth scanning, combined with uncertainties in beam pointing, reduce the accuracy of detection data; particularly when the values of dual-polarization parameters are small, the errors introduced by such systems often mask the true characteristics of atmospheric echoes.

To filter out non-meteorological echoes, the Cylindrical Polarimetric Phased Array Radar (CPPAR) developed by the University of Oklahoma suppresses non-meteorological echoes generated by mountains and buildings (Li et al., 2023). At X-band frequencies, severe signal attenuation in precipitation areas and the difficulty in identifying natural targets such as dry snow above the freezing level further complicate the calibration process (Du et al., 2013). Many researchers have improved data usability by correcting reflectivity factors (Z_H) and Z_{DR} (Matsuda and Onishi, 2019; Bringi et al., 1990; Burgemeister et al., 2024; Jha et al., 2024).

To address systematic biases, researchers worldwide have developed a variety of quality control and calibration approaches. Among them, the method using light rain observations from vertical birdbath scans as natural calibration targets represents a relatively effective solution for Z_{DR} bias correction; however, many radars are unable to perform scans at a 90° elevation angle. Ryzhkov et al. (2005) proposed a method based on collecting Z_{DR} values for dry snow at elevation angles between 40° and 60°, achieving an accuracy of 0.2 dB for Z_{DR} data. Although early studies attempted end-to-end calibration using tethered metal spheres (Williams et al., 2013) or UAV field calibration (Yin et al., 2021), these methods are difficult to meet real-time operational requirements due to high costs and environmental constraints. Currently, China lacks unified standards for dual-polarization phased-array radar testing. Pre-shipment unit testing often overlooks the effects of transportation and installation losses as well as the impact of the radome on gain, leading to discrepancies in detection results for the same target across different radars. Sanchez-Rivas et al. (2022) utilized quasi-vertical profile calibration to calibrate the radar Z_{DR} with an accuracy of 0.1 dB. Since 2022, the German Weather Service has adopted a comprehensive monitoring strategy that combines vertical pointing scans (birdbath scans) performed every 5 minutes, continuous analysis of solar radiation data, and single-point calibration techniques, successfully controlling Z_{DR} deviations within a high-precision range of ±0.1 dB (Frech et al., 2020).

https://doi.org/10.5194/egusphere-2026-3965
Preprint. Discussion started: 28 August 2026
© Author(s) 2026. CC BY 4.0 License.

In addition to the issues mentioned above, the most serious problem with phased-array weather radars is that detection performance deteriorates when the radar beam deviates from the normal to the array plane (Zhu et al., 2025; Zhang et al., 2009; Heberling et al., 2020). This leads to a decline in Z_{DR} detection performance as the elevation angle increases, and different scanning modes also result in variations in Z_{DR} detection. Meanwhile, many authors have evaluated the detection performance of phased-array weather radars by comparing their data with that from other radar types. For example, Heberling et al. (2018), who conducted a joint operation between the X-band phased-array weather radar provided by Raytheon to the University of Massachusetts and a mechanically scanned polarized X-band weather radar to evaluate the polarization measurement performance of the X-band phased-array weather radar. The cross-polarization mode of phased-array weather radars affects the data. Zhang et al. (2021) effectively addressed the calibration issue of dual-polarization phased-array weather radars by performing spatiotemporal matching with S-band radar data to correct Z_H and Z_{DR} data at different elevation angles and time points. This approach largely eliminated the effects of variations in phased-array antenna transmit/receive gain and beamwidth caused by elevation angle deviations from the array normal (Zhang et al., 2021). Two polarimetric phased-array weather radars developed by the Advanced Radar Research Center (ARRC) at the University of Oklahoma, namely the Cylindrical Polarimetric Phased Array Radar (CPPAR) and the Planar Polarimetric Phased Array Radar (PPPAR, codenamed Horus), were compared with the WSR-88D. The planar PPAR (Horus) exhibits inherent drawbacks such as enlarged polarimetric variable errors, sensitivity degradation, and deteriorated polarization purity during wide-angle electronic scanning when the beam deviates from the normal direction (off-broadside); however, no algorithmic correction scheme has been proposed (Ho et al., 2025). As a two-dimensional phased array radar, Horus faces significant challenges in calibrating polarization measurement variables to meet weather observation requirements (Zrnic et al., 2011; Zhang et al., 2016). Polarization losses are difficult to effectively compensate for and calibrate, posing difficulties in achieving high-quality polarization weather measurements (Dorsey et al., 2022; Fulton et al., 2022; Ivic et al., 2023; Zhang, 2009). As the scan angle changes, the CPI of a polarization phased array radar (PPAR) also changes, leading to distorted estimates of the target polarization scattering matrix (PSM). He et al. (2023) proposed a system-optimization-based bias correction method that significantly reduces the Z_{DR} bias to approximately 0.1 dB, meeting operational requirements.

To address the aforementioned challenges, this study proposes a refined method for correcting Z_{DR} data from phased-array weather radars. This method no longer relies on complex external hardware; instead, it corrects Z_{DR} data by addressing system bias and attenuation in the XPAR, simulating a dual-polarization microstrip antenna array at 9.4 GHz using High Frequency Structure Simulator (HFSS), and compensating for isolation degradation. Due to the influence of isolation, this study selects light rain as a natural target and applies weighting to three elevation angles where the beam pointing angle is close to 0°. By combining HFSS simulation results with XPAR measurement data, this study analyzed the variation patterns of antenna gain and 3 dB beamwidth as a function of v; based on the quadratic relationship between phased array antenna gain and beam angle, the Quadratic Correction Method (QCCPI) was employed to compensate for deviations in cross-polarization isolation between different elevation angles. This study applies Z_{DR} correction to XPAR data from the Guangdong region of China. This refined correction method not only rapidly and intuitively reflects the variation in radar detection performance as

https://doi.org/10.5194/egusphere-2026-3965
Preprint. Discussion started: 28 August 2026
© Author(s) 2026. CC BY 4.0 License.

elevation increases but also effectively distinguishes between systematic errors and parameter changes caused by precipitation attenuation.

A squall line is a linear convective band composed of thunderstorm clouds (ordinary cells or supercells) and represents a mesoscale convective system with intense convection. It can extend from several tens to several hundreds of kilometers in length, and typically spans the entire troposphere. Its lifetime ranges from a few hours to more than ten hours. On weather radar imagery, a squall line resembles a "skewer" linking a series of thunderstorms or cumulonimbus clouds. Such systems have been documented in various regions, including the Maritime Continent of Southeast Asia (Diong et al., 2026), West Sumatra (Lopez-Bravo et al., 2026), South China (Chen et al., 2026), and South Korea (Swastiko et al., 2026). In this study, we focus on a summer squall line observed by an X-band phased-array radar (XPAR) in Guangdong, China. The proposed RC-Z_{DR} algorithm is applied to correct the Z_{DR} data, which play a critical role in identifying the phase states of hydrometeors within the vertical structure of the squall line.

This refined correction scheme not only clearly illustrates how radar detection performance changes with increasing elevation angle but also effectively distinguishes between changes in polarization parameters caused by systematic errors and those caused by precipitation attenuation. In this paper, the corrected XPAR data were spatially and temporally matched with operational S-band dual-polarization weather radar (SPOL). The results demonstrate that this method exhibits good accuracy and stability in capturing the fine-scale structure of severe convective systems, providing a scientific and efficient technical solution for operational quality control and performance evaluation of next-generation phased-array weather radars.

2 Materials and Methods

2.1 Data Introduction

2.1.1 X-Band Phased-Array Weather Radar

As shown in Fig. 1, the data used in this study were obtained from 8 X-band Phased-Array Weather Radars (XPAR) and 1 S-band Dual-Polarization Weather Radars (SPOL) located in Guangdong Province, China. These radars can operate in narrow-transmit/narrow-receive single-beam (NT/NR-SB) mode or wide-transmit/narrow-receive multi-beam (WT/NR-MB) mode. Different XPAR units employ distinct scanning modes and numbers of elevation angles; the specific parameters are detailed in Table 1.

https://doi.org/10.5194/egusphere-2026-3965
Preprint. Discussion started: 28 August 2026
© Author(s) 2026. CC BY 4.0 License.

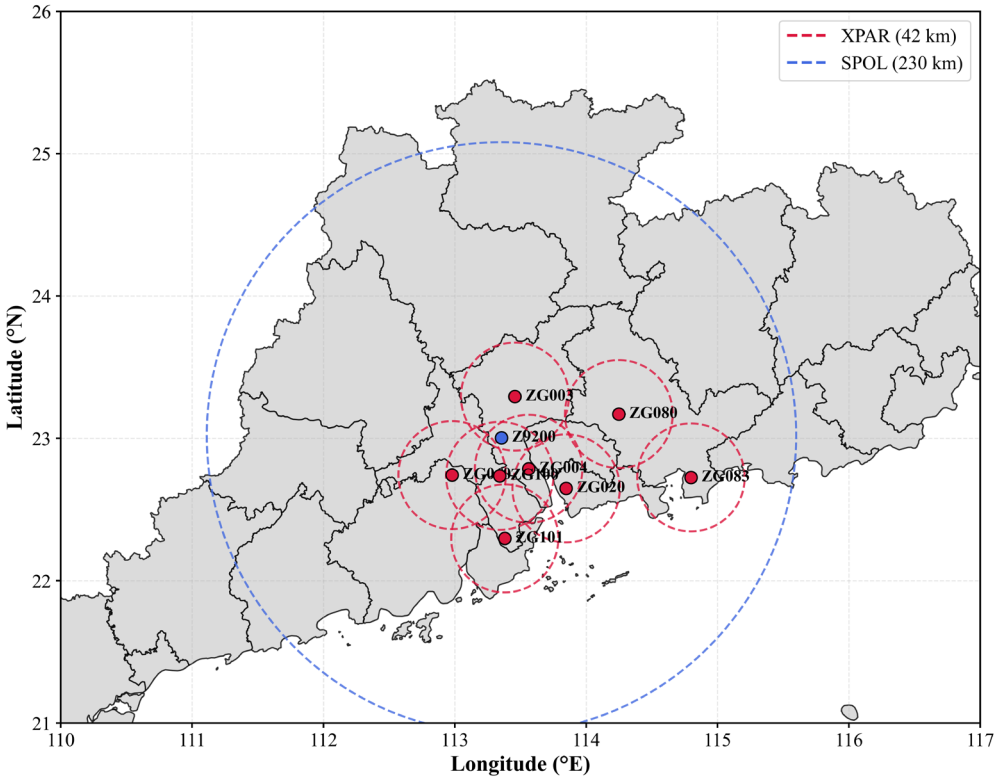

Figure 1. Distribution Map of XPAR and SPOL in Guangdong Province.

XPAR is an advanced weather radar system serving as a primary tool for detecting mesoscale and microscale weather events. Leveraging its high spatiotemporal resolution, it can complete a volume scan within 60 to 92 seconds. By employing phase-controlled scanning—specifically electronic scanning for elevation and mechanical scanning for azimuth—the radar acquires dual-polarization parameters to capture finer echo structures. The beam pointing angle is -15°, and parameters such as peak transmit power, volume scan time, elevation coverage, and beamwidth vary across different operation modes. As shown in Fig. 2, the XPAR units utilized in this study were manufactured by Guangdong Naruida Radar Applications Technology Company Limited. The XPAR provides several key variables, including reflectivity (Z_H), differential reflectivity (Z_{DR}), differential phase (Φ_{DP}), specific differential phase (K_{DP}), radial velocity (V), and spectrum width (W). Since 2022, to meet the requirements for refined detection, several radar stations in Guangdong have been upgraded to wide-transmit/narrow-receive (WTNR) mode. This mode utilizes multi-beam scanning (see Table 1), increasing the number of observation elevations from 16 to 68 layers and improving the elevation resolution from 1.8° to 0.9°.

https://doi.org/10.5194/egusphere-2026-3965
Preprint. Discussion started: 28 August 2026
© Author(s) 2026. CC BY 4.0 License.

Figure 2. X-Band Phased Array Weather Radar.

Table 1. Parameters of XPAR and SPOL.

Radar Parameters	XPAR	SPOL
Operating Frequency	9.3 GHz~9.5 GHz	2.8 GHz
Peak Power	256 W	⩾650 kW
Temporal Resolution	92 s	360 s
Maximum detection range	42 km	230 km
Range Resolution	30 m	250 m
Beamwidth	3°	0.95°
Volume Scan Mode	VRHI	VPPI
Array preset elevation angle	15°	——
Polarization Scheme	Dual-polarization, Simultaneous Transmit and Receive (STAR)	Dual-polarization, STAR
Number of Elevation Layers	12, 16, 40, 68 layers	0.5° ~19.5°

2.1.2 S-band Dual-Polarization Weather Radar

The S-band dual-polarization weather radar (SPOL), serving as the ground truth for weather radar observations, has been put into operational use (Zhou et al., 2022). However, it features relatively low spatiotemporal resolution, completing a volume scan every 6 minutes with a spatial range resolution of 230 m. The scan includes nine elevation angles: 0.48°, 1.49°, 2.41°, 3.30°, 4.30°, 6.02°, 9.89°, 14.59°, and 19.51°. Beyond measuring traditional radar reflectivity, SPOL can simultaneously transmit electromagnetic waves in both horizontal (H) and vertical (V) polarizations to detect more comprehensive atmospheric information. Consequently, SPOL is capable of capturing the size, shape, and orientation of precipitation targets within the radar sampling volume.

https://doi.org/10.5194/egusphere-2026-3965
Preprint. Discussion started: 28 August 2026
© Author(s) 2026. CC BY 4.0 License.

2.2 Method Introduction

2.2.1 Refined Correction Method for ZDR of XPAR (RC-Z_{DR})

Fig. 3 provides a comprehensive overview of XPAR's refined Z_{DR} correction algorithm (RC-Z_{DR}), which is divided into five stages from top to bottom: data extraction, radial interference filtering and attenuation correction, system bias correction, cross-polarization isolation correction, and result evaluation. During the data extraction stage, particles from light rain, moderate rain, and severe convective events are identified, and samples from light and moderate rain below the zero-degree layer are selected. System bias correction, cross-polarization isolation correction, and preliminary validation are then performed in sequence; Radial interference is identified and removed using a comprehensive filtering method; system bias correction is based on data from light rain periods, employing the Bias-WZ_{DR} method to determine the sign and magnitude of the bias; Cross-polarization isolation correction first utilized HFSS electromagnetic simulation to analyze how antenna gain and 3dB beamwidth vary with beam pointing angle, then combined this with the QCCPI method to calculate the average Z_{DR} compensation value for each elevation angle layer and complete the correction; Finally, based on heavy precipitation particle data, an XPAR squall line event was corrected using the RC-Z_{DR} method and validated using SPOL.

$$Z'_{\mathrm{DR}}(\mathrm{r}) = Z_{\mathrm{DR}}(\mathrm{r}) + 2\int_0^r A_{\mathrm{DP}}(\mathrm{s})ds, \tag{1}$$

$$A_H = \begin{cases} \alpha_1 K_{\mathrm{DP}}, \delta_1 < K_{\mathrm{DP}} < \delta_2 \\ \lambda_1 Z_H^{\gamma_1}, K_{DP} \le \delta_1 \text{或} K_{\mathrm{DP}} \ge \delta_2 \end{cases}, \tag{2}$$

$$A_{DP} = \begin{cases} \alpha_2 K_{\mathrm{DP}}, \delta_1 < K_{\mathrm{DP}} < \delta_2 \\ \lambda_2 A_{\mathrm{H}}^{\gamma_2}, K_{\mathrm{DP}} \le \delta_1 \text{或} K_{\mathrm{DP}} \ge \delta_2 \end{cases}, \tag{3}$$

In this case, γ_1=0.779 (Matrosov et al., 2008). Since γ_2 varies little, we take it as a constant of 1.13; Matrosov et al. (2002) determined a_1 to be 0.22 dB/deg in the X-band based on field tests, and we use two thresholds: δ_1=0.1 and δ_2=3.0 (Matrosov et al., 2008).

The comprehensive threshold method used in this study employs the following statistical anomaly criteria: when the Z_{DR} is greater than or equal to 3 dB and the differential phase shift rate (K_{DP}) falls within the range of -0.1 to 0.15, the data point is classified as anomalous.

https://doi.org/10.5194/egusphere-2026-3965
Preprint. Discussion started: 28 August 2026
© Author(s) 2026. CC BY 4.0 License.

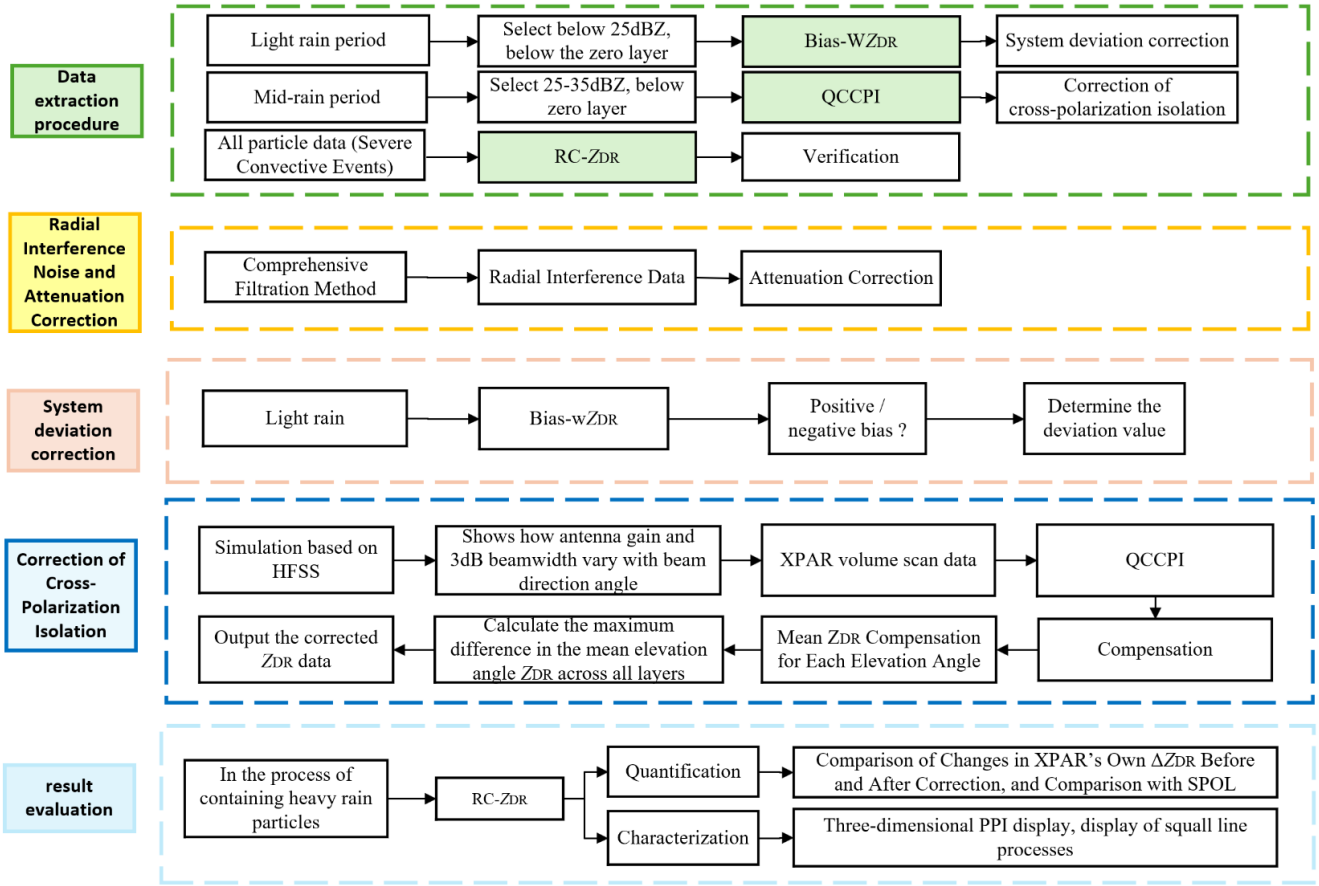

Figure 3. RC-Z_{DR} Algorithm Flowchart.

2.2.2 ZDR system bias correction method based on beam pointing angle weighting（Bias-WZ_{DR}）

Conventional weather radars typically employ the natural target method for Z_{DR} system bias correction, which uses the mean Z_{DR} at the highest elevation angle as the overall system bias. For XPAR, due to antenna isolation effects, observations at the maximum detectable elevation angle of 20.7° exhibit significant biases and cannot be used for system bias calibration. Therefore, in practice, the elevation angles corresponding to the beam pointing angle 0° are prioritized, as at these directions the bias introduced by isolation is minimized.

In this study, the array preset elevation angle of the XPAR is set to 15°. The actual elevation angle sequence is 0.9°, 2.7°, 4.5°, 6.3°, 8.1°, 9.9°, 11.7°, 13.5°, 15.3°, 17.1°, 18.9°, and 20.7°. As shown in Eq. (5), this quantifies the relationship among the beam pointing angle, the actual elevation angle of XPAR, and the array preset elevation angle. The calculated beam pointing angles (θ_p) corresponding to each elevation angle are: -14.1°, 12.3°, -10.5°, -8.7°, -6.9°, -5.1°, -3.3°, -1.5°, 0.3°, 2.1°, 3.9°, and 5.7°. To mitigate observation errors caused by isolation, the three beam pointing angles closest to 0° are selected for analysis: -1.5°, 0.3°, and 2.1°.

https://doi.org/10.5194/egusphere-2026-3965
Preprint. Discussion started: 28 August 2026
© Author(s) 2026. CC BY 4.0 License.

Since 0.3° is the closest to 0° and has the lowest cross-polarization isolation, a system bias correction method based on weighting Z_{DR} data from three elevation angles near the 0° beam direction is proposed (Bias- WZ_{DR}). The calculation process for Bias-WZ_{DR} is as follows:

1. First, select the light rain particles

According to the dual-polarization theory, light raindrops are spherical, have a uniform shape and phase, and are isotropic, with Z_{DR}≈0 dB. Z_{DR} is calculated using Eq. (4) from the horizontal reflectance factor and the vertical reflectance factor, with units in dB. The criteria for light rain (Wen et al., 2025) are: (1)Z_H<25 dBZ, (2) ρ_{hv}>0.97, and (3) below the zero-degree layer h_0.

$$Z_{\mathrm{DR}} = 10\log_{10}\left(\frac{Z_{HH}}{Z_{VV}}\right), \tag{4}$$

2. Determine the height of the zero-degree layer

As shown in Fig. 4, first obtain a layered cloud data analysis from XPAR and retrieve its PPI image at a 20.7° elevation angle. It can be observed that near the bright band of the zero-degree layer, Z_H increases, ρ_{hv} decreases, and Z_{DR} rises, forming a distinct "semi-annular" pattern (Wang et al., 2024) at an altitude close to the zero-degree isotherm. Above the zero-degree layer, water condensation typically takes the form of ice crystals, snowflakes, and other ice phases, while within the zero-degree layer, it is often in a mixed-phase state; below the zero-degree layer, small raindrops are typically spherical, and Z_{DR} data from dual-polarization radar are close to 0.

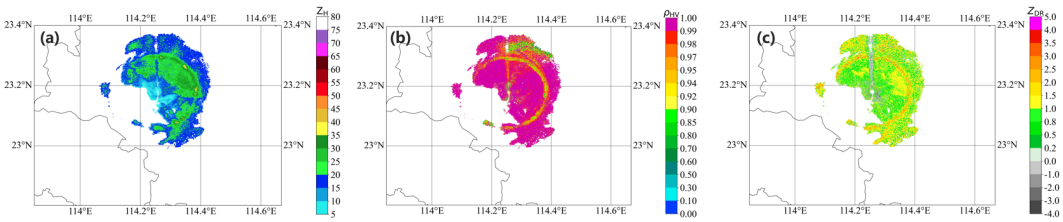

Figure 4. ZG080XPAR, September 6, 2024, 07:57:44, PPI images at a 20.7° elevation angle (a) Z_H, (b)$\boldsymbol{\rho_{hv}}$, (c) Z_{DR}

As shown in Fig. 5, the RHI image allows us to observe the variations in Z_H and ρ_{hv} as particles move through the 3.8 km to 5 km altitude layer. Below the zero-degree layer, ice crystals form a liquid film as they fall, making them more prone to collision and coalescence. To avoid the influence of the solid-liquid mixture near the zero-degree layer, it is best to select pure light rain data from the 1 km layer below the zero-degree layer. To prevent the impact of ground clutter, pure light rain data at a certain altitude above the ground must also be selected. Therefore, the pure light rain data selected in this paper has an altitude h_0 of 1-2.8 km.

https://doi.org/10.5194/egusphere-2026-3965
Preprint. Discussion started: 28 August 2026
© Author(s) 2026. CC BY 4.0 License.

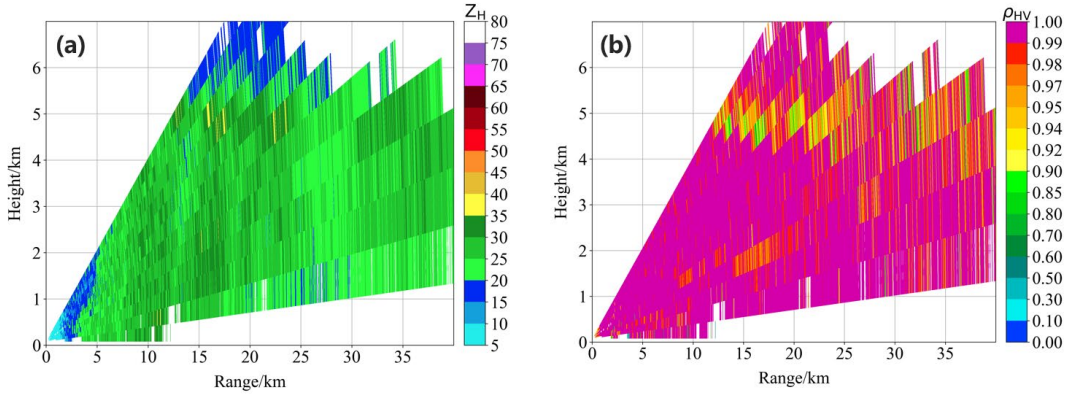

Figure 5. RHI images of ZG080 at azimuth 50° (a) Z_H, (b) $\boldsymbol{\rho_{hv}}$.

3. Calculate the weighted sum of the Z_{DR} mean values for the beam angles of -1.5°, 0.3°, and 2.1°.

This method assigns different weights to the mean Z_{DR} data from the three elevation angles: because 0.3° is closest to 0°, the weight at 0.3° is 0.6; while the beam angles of -1.5° and 2.1° are assigned a weight of 0.2. The final composite mean is the Z_{DR}.

$$\theta_p = \theta_{act} - \theta_{pre} , \tag{5}$$

In this case, the θ_{pre} value for the XPAR is 15°. θ_{act} refers to the actual detection elevation angle of the XPAR, while θ_{pre} is the beam pointing angle.

$$\overline{Z_{DR}} = w1Z_{DR1} + w2Z_{DR2} + w3Z_{DR3} , \tag{6}$$

where w1=0.2, w2=0.6, w3=0.2, Z_{DR1}、Z_{DR2} and Z_{DR3} are the mean Z_{DR} values at beam angles of -1.5°, 0.3°, and 2.1°, respectively.

2.2.3 HFSS Simulation of Beam Characteristics for Dual-Polarization Phased Array Antennas and the QCCPI Algorithm

Phased-array weather radars feature superior beam agility compared to conventional mechanically scanned radars, enabling rapid detection of weather systems. However, when the beam steering angle deviates from the array boresight, key parameters including the 3 dB beamwidth, antenna gain and sidelobe level will vary. Consequently, the conventional weather radar equation is no longer applicable to calculate the echo power of phased-array weather radars, and a revised radar equation that accounts for beam steering angle is required. For dual-polarization phased-array weather radars, polarimetric parameters are inherently small in magnitude, so beam deviation from the array boresight induces much larger errors in these polarimetric variables. Prior to deriving the meteorological radar equation for phased-array systems, we first analyzed the traditional single-target weather radar (Fišer et al., 2022) described by Eq. (7).

https://doi.org/10.5194/egusphere-2026-3965
Preprint. Discussion started: 28 August 2026
© Author(s) 2026. CC BY 4.0 License.

$$P_r = \frac{P_t G^2 \lambda^2 \sigma}{(4\pi)^3 r^4 L_s L_a}, \tag{7}$$

Where P_r represents the received power, L_a is the atmospheric transmission loss, L_a is the radar system loss, r is the distance from the target to the radar, σ is the radar cross section, λ is the antenna wavelength, G is the antenna gain, and P_t the transmitted power.

As can be seen from Eq. (7), the conventional single-target meteorological radar equation assumes that the radar gain remains constant; however, in phased-array radar, the antenna gain G changes as the beam deviates from the normal to the array plane. For a phased-array weather radar with a beam deviating from the normal to the array plane, the transmission gain of the array antenna is G_t, and the receive gain is G_r (Zhang et al., 2011). Here, G_{t0} is the transmit gain when the beam is aligned with the array plane normal, G_{r0} is the receive gain when the beam is aligned with the array plane normal, and θ is the angle by which the beam deviates from the array plane normal. Therefore, the single-target meteorological radar equation for a phased-array radar is given by Eq. (10):

$$G_t = G_{t0} \cos\theta , \tag{8}$$

$$G_r = G_{r0} \cos\theta , \tag{9}$$

$$P_r = \frac{P_t G_{t0} G_{r0} (\frac{\lambda_0}{\lambda})^4 (\cos\theta)^2 \lambda^2 \sigma}{(4\pi)^3 r^4 L_s L_a}, \tag{10}$$

where (λ_0/λ) is the frequency offset.

After discussing the meteorological equation for a single-target phased-array radar, we should now consider the meteorological equation for a multi-target phased-array radar. Since multiple targets occupy a certain volume, factors such as the 3 dB beamwidth and pulse width must be taken into account in the meteorological equation for a multi-target phased-array radar. Zhang et al. (2011) derived the following meteorological equation for phased-array radar Eq. (11):

$$\overline{P_r} = \frac{\pi^3}{1024 \ln 2} \frac{P_t G_{t0} G_{r0} h \varphi_h \varphi_v \cos\theta}{\lambda^2} \frac{|K|^2}{r^2} Z , \tag{11}$$

Where: h is the radar transmission pulse width, φ_h is the horizontal 3dB reception beamwidth, φ_v is the vertical 3 dB reception beamwidth, Z is the reflectivity factor, and $|K|^2$, where m is the complex refractive index.

$$|K|^2 = |(m^2 - 1)/(m^2 + 2)|^2 , \tag{12}$$

Since the XPAR used in this paper is a one-dimensional phased-array radar that employs electronic scanning in the elevation angle and mechanical scanning in the horizontal azimuth, under ideal conditions, when the radar performs electronic scanning in the elevation direction, all other radar parameters remain constant, and only the gain G and the 3 dB beamwidth φ change. This ultimately results in the following deviation in Z_{DR}, as shown in Eq. (13):

$$\Delta Z_{DR} = 2(G_h - G_v) + 10 \log_{10}(\varphi_h/\varphi_v) , \tag{13}$$

https://doi.org/10.5194/egusphere-2026-3965
Preprint. Discussion started: 28 August 2026
© Author(s) 2026. CC BY 4.0 License.

In the Eq. (13): ΔZ_{DR} is the error between the Z_{DR} measured by the radar and the true value; G_h is the receiving gain of the horizontal polarization channel of the XPAR radar; and $G_v$is the receive gain of the vertical polarization channel.

Figure 6 shows a top view of the antenna elements in the antenna array simulated using High Frequency Structure Simulator (HFSS) in this study (An et al., 2023). This antenna element is a dual-polarization microstrip patch antenna operating at 9.4 GHz.

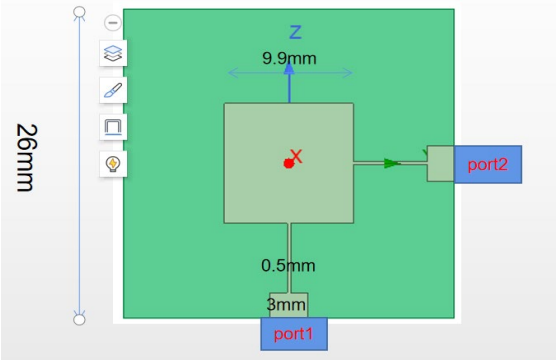

Figure 6. Top view of a dual-polarization microstrip patch antenna.

Figure 7 shows the antenna array layout, consisting of 30 elements in the horizontal direction, spaced 22 mm apart, and 56 elements in the vertical direction, spaced 22 mm apart.

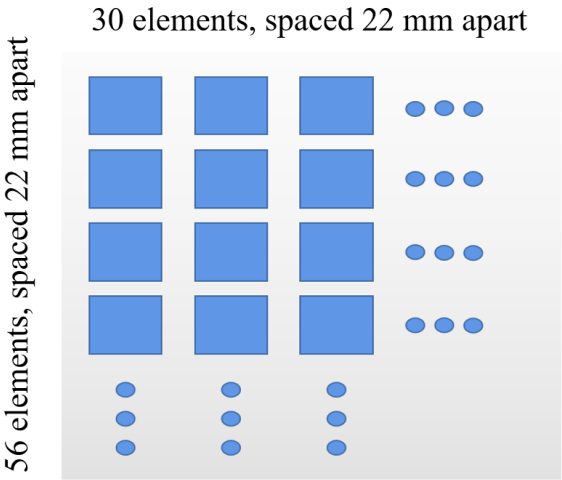

Figure 7. Antenna Array Layout Diagram.

Currently, the antenna array gain of most dual-polarization phased-array weather radars exceeds 36 dB. To achieve a high antenna array gain, either the gain of each antenna element must be sufficiently high, or the number of antenna elements must be sufficiently large. In the simulation experiments conducted in this paper, the gain of a single antenna element reached 8.1 dB, as shown in Fig. 8:

https://doi.org/10.5194/egusphere-2026-3965
Preprint. Discussion started: 28 August 2026
© Author(s) 2026. CC BY 4.0 License.

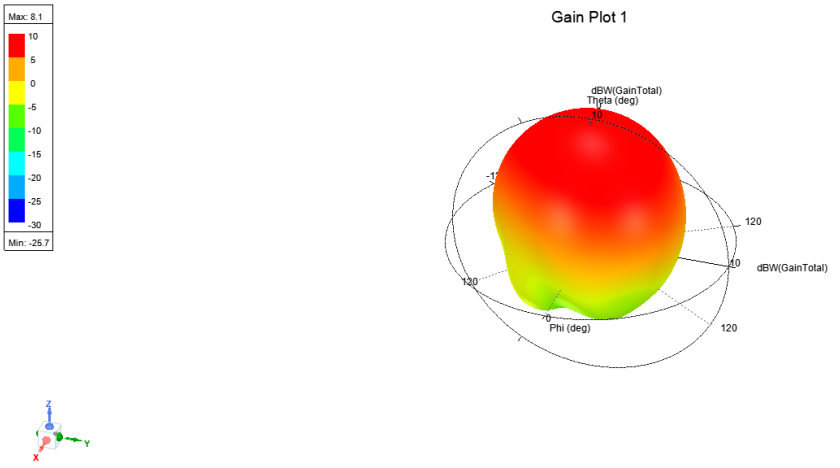

Figure 8. Gain Chart for a Dual-Polarization Microstrip Patch Antenna.

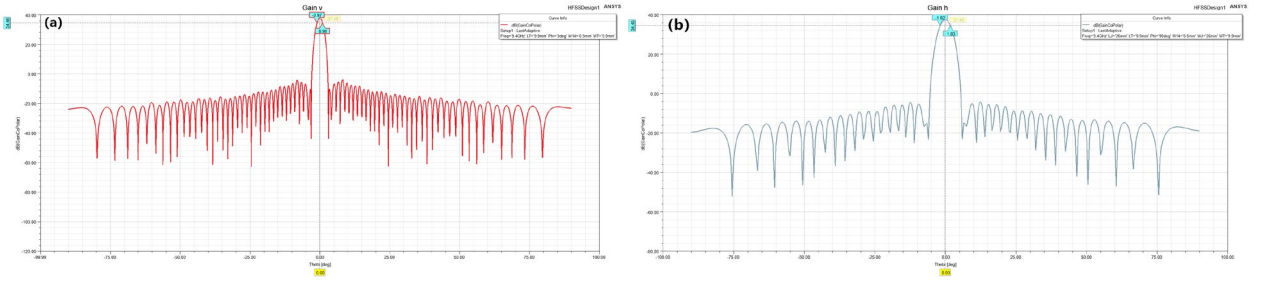

Figure 9. (a) Vertical gain pattern and (b) horizontal gain pattern for the array antenna with a beamwidth of 0°.

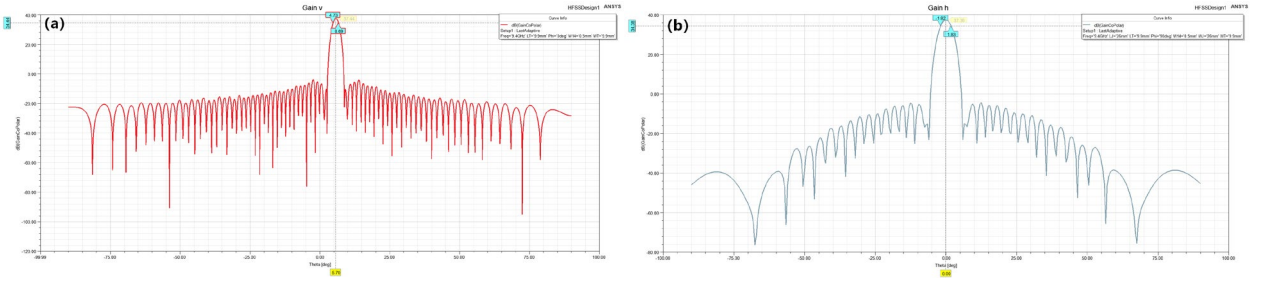

Figure 10. (a) Vertical gain pattern and (b) horizontal gain pattern for the array antenna with a beamwidth of 5.7°.

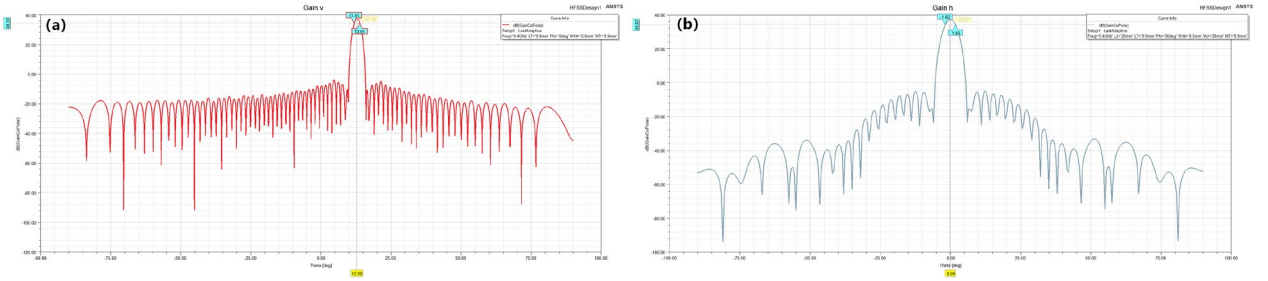

https://doi.org/10.5194/egusphere-2026-3965
Preprint. Discussion started: 28 August 2026
© Author(s) 2026. CC BY 4.0 License.

Figure 11. (a) Vertical gain pattern and (b) horizontal gain pattern for the array antenna with a beamwidth of 12.9°.

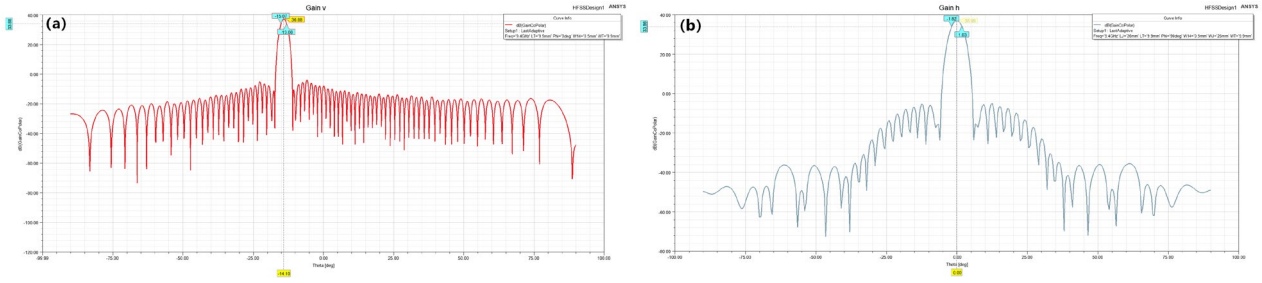

Figure 12. (a) Vertical gain pattern and (b) horizontal gain pattern for the array antenna with a beamwidth of -14.1°.

The horizontal 3dB beamwidth of this antenna array is 3.65° at boresight, with a horizontal antenna gain of 37.45 dB; the vertical 3dB beamwidth is 1.95°, with a vertical antenna gain of 37.46 dB. The initial first sidelobe level of this array antenna was rather high. After applying Hamming window weighting, the first sidelobe level is reduced to approximately −40 dB, albeit at the cost of reduced radiated power. This array antenna generally meets the performance requirements of most dual-polarization phased-array weather radars in the meteorological field.

The bias of the Z_{DR} at boresight is calculated to be approximately 2.70 dB according to Eq. (13). Using this Z_{DR} value as the reference, simulations are further carried out to determine the difference relative to the reference value when the beam is steered off the boresight of the array face.

Table 2. Table of Beam Parameters at Different Pointing Angles.

Beam pointing angle /°	φ_h/°	φ_v/°	G_h/dB	G_v/dB	$2(G_h\text{-}G_v)$	$10\log_{10}(G_h/G_v)$
-14.1	3.65	2.01	36.98	36.88	0.2	2.59
-12.3	3.65	1.99	37.09	37.00	0.18	2.63
-10.5	3.65	1.98	37.19	37.11	0.16	2.65
-8.7	3.65	1.97	37.27	37.21	0.12	2.68
-6.9	3.65	1.97	37.33	37.28	0.10	2.68
-5.1	3.65	1.96	37.39	37.35	0.08	2.70
-3.3	3.65	1.95	37.43	37.41	0.04	2.72
-1.5	3.65	1.95	37.45	37.44	0.02	2.72
0	3.65	1.95	37.45	37.46	-0.02	2.72
0.3	3.65	1.95	37.45	37.46	-0.02	2.72
2.1	3.65	1.95	37.45	37.46	-0.02	2.72
3.9	3.65	1.95	37.42	37.46	-0.08	2.72
5.7	3.65	1.96	37.38	37.44	-0.12	2.70
7.5	3.65	1.97	37.32	37.40	-0.16	2.68
9.3	3.65	1.97	37.25	37.34	-0.18	2.68
11.1	3.65	1.98	37.16	37.27	-0.22	2.65

https://doi.org/10.5194/egusphere-2026-3965
Preprint. Discussion started: 28 August 2026
© Author(s) 2026. CC BY 4.0 License.

12.9	3.65	2.00	37.07	37.18	-0.22	2.61

The values in the "beam pointing angle" column of Table 2 are specified relative to the array normal and in the vertical direction; for example, -14.6° indicates that the beam starts from the array normal and moves 14.6° toward the ground. A value of 12.9° indicates that the beam starts from the array normal and moves 12.9° toward the sky. Combining the beam parameters for different azimuth angles in Table 2, which were simulated using HFSS, Figure 13 plots the deviation Z_{DR} for different azimuth angles (after subtracting the 2.70 dB deviation of the Z_{DR} at the 0° beam pointing angle) based on Eq. (13).

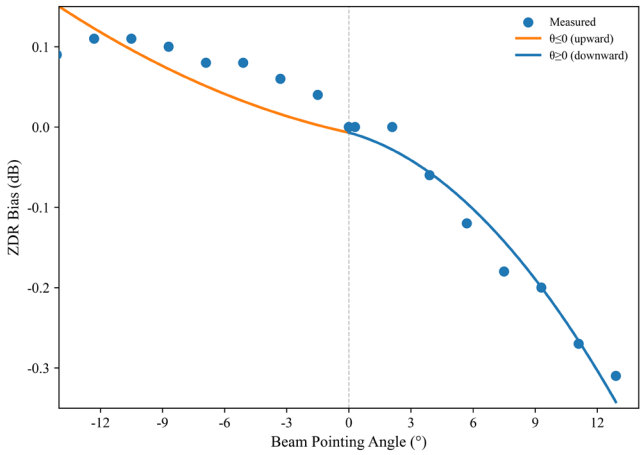

Figure 13. Z_{DR} deviation at different beam pointing angles.

As can be seen from Fig. 13, the Z_{DR} bias decreases approximately in accordance with a quadratic curve when the beam steering angle is greater than 0°, whereas it rises following a similar quadratic trend when the beam steering angle is less than 0°. The patch elements adopted in this simulation are microstrip patch antennas, which feature an asymmetric physical structure: one side is equipped with microstrip feed lines while the other side is not. For this reason, the variation characteristics of Z_{DR} bias differ when the beam deviates from the normal direction of the array face in different directions. Nevertheless, the Z_{DR} bias in both angular directions presents a common rule — its increase or decrease basically complies with the variation law of a quadratic curve.

Therefore, this paper proposes a quadratic curve fitting-based method to compensate for the degradation of Z_{DR} cross-polarization isolation (QCCPI). The steps are as follows:

1. First, data from a selected radar site are traversed over a certain time period with a starting index of 1, a step size of 4, and a total of N=10 volume scans. The step size of 4 is primarily used to eliminate errors caused by the proximity of consecutive time frames.

$$file_{idx_k} = start + k \times step, k = 0,1,2 \cdots N - 1\,, \tag{14}$$

2. The actual Z_{DR} mean values detected by XPAR every 6 minutes, plotted against the pointing angle, exhibit a quadratic trend similar to the HFSS simulation. When the beam pointing angle deviates from the array normal, the mean Z_{DR} shows

https://doi.org/10.5194/egusphere-2026-3965
Preprint. Discussion started: 28 August 2026
© Author(s) 2026. CC BY 4.0 License.

a gradually decreasing trend. Ignoring the effects of ground clutter and other external factors such as the radar dome, based on the symmetry in Eq. (15), the Z_{DR} reaches its maximum or minimum at $\theta = 0°$。

$$Z_{\mathrm{DR}}(\theta) = Z_{\mathrm{DR}}(-\theta), |\theta < 90°| , \tag{15}$$

3. Based on the above analysis, a quadratic function is chosen to fit the data. The expression of the quadratic curve is:

$$Z_{\mathrm{DR}}(\theta) = -\alpha(\theta - \beta)^2 + \gamma , \tag{16}$$

4. Because$Z_{\mathrm{DR}}(-\theta) = Z_{\mathrm{DR}}(\theta)$， we have$\beta$=0 and $\gamma = Z_{DR}(0)$. The quadratic curve is then expressed as:

$$Z_{\mathrm{DR}}(\theta) = -\alpha\theta^2 + Z_{\mathrm{DR}}(0) , \tag{17}$$

5. After calculation, the coefficient α for a specific site is obtained such that the sum of squared errors between the mean values and the fitted values is minimized. $Z_{\mathrm{DR}}(0)$ is the original Z_{DR} value of the measured raindrops, $-\alpha\theta^2$ is the Z_{DR} error after the beam pointing angle deviates from the array normal by θ， and $Z_{\mathrm{DR}}(\theta)$ is the actually detected Z_{DR} value. Once the expression is obtained, the Z_{DR} can be compensated by simply adding $-\alpha\theta^2$：

$$Z_{\mathrm{DR}}^{corr} = Z_{\mathrm{DR}}^{obs} + (-\alpha\theta^2) , \tag{18}$$

Z_{DR}^{corr} denotes the corrected value at each elevation angle, while Z_{DR}^{obs} represents the observed value from the XPAR base data.

6. Finally, for the Z_{DR} variation with pointing angle measured within a single time period, the difference between its maximum and minimum values is calculated. A larger variation indicates poorer cross-polarization isolation performance of the antenna or worse system stability. This metric can be used to monitor the health status of XPAR Z_{DR} data, and its effectiveness is demonstrated in Sec. 3.

$$\Delta Z_{\mathrm{DR}} = \max_{\theta}(Z_{\mathrm{DR}}(\theta)) - \min_{\theta}\big(Z_{\mathrm{DR}}(\theta)\big), \tag{19}$$

Here, θ covers all elevation angles.

2.3 Dataset

2.3.1 XPAR systematic bias correction dataset

Table 3 summarizes the main factors affecting the quality of Z_{DR} data from XPAR radars. XPAR observations are prone to interference from various non-meteorological echoes, such as isolated point clutter and ground clutter, which are evident at Station ZG061. Corresponding quality control procedures are implemented to eliminate the aforementioned interferences. Furthermore, the light rain method is adopted to correct the systematic bias of XPAR measurements. A quadratic function is fitted to compensate for the observational errors caused by the degradation of cross-polarization isolation.

https://doi.org/10.5194/egusphere-2026-3965
Preprint. Discussion started: 28 August 2026
© Author(s) 2026. CC BY 4.0 License.

In addition, Table 3 lists the XPAR radars used in this study, including the time, station information (ZG003, ZG004, ZG020, ZG020, ZG060, ZG080, ZG083, ZG100, ZG101), and the Z_{DR} results before and after system bias correction.

Table 3. XPAR System Bias Correction.

Time (s)	Site	$Z_{DR_bias(dB)}$	$Z_{DR_bias_cor(dB)}$
20230327075510-081235	ZG003	-0.207	-0.397
20230327062555-064928	ZG004	-0.622	0.041
20230614000005-003047	ZG020	1.182	-0.286
20230327052747-055221	ZG060	-2.148	0.242
20230327060535-063752	ZG080	0.588	-0.186
20230613201453-205449	ZG083	0.963	0.244
20230616145915-152958	ZG100	-1.015	0.383
20230327051630-054845	ZG101	0.302	-0.121

2.3.2 Dataset for correcting the deterioration of cross-polarization isolation of the XPAR

Table 4 summarizes the dataset used to analyze the deterioration of cross-polarization isolation for the XPAR radar. This dataset consists of simultaneous observations acquired after the systematic bias correction of the XPAR system, covering the same observation period as the bias correction dataset. Moderate rain hydrometeors are selected as the research objects, with specific screening criteria set as follows: horizontal reflectivity ranging from 25 dBZ to 35 dBZ and cross-correlation coefficient ρ_{hv} greater than 0.95. Moderate rainfall is chosen because its Z_{DR} can more distinctly reflect the variations in Z_{DR} values caused by different elevation angles. Light rain is excluded since its Z_{DR} is close to zero, making such variations undetectable. Heavy rain is also ruled out, as its hydrometeors produce excessively large Z_{DR} fluctuations, and signal attenuation introduces substantial additional errors.

Table 4 shows the maximum elevation angle error of XPAR's Z_{DR} after applying isolation correction to the moderate rain data for each time period. It can be seen that the corrected Z_{DR} values have decreased compared to those before correction; some of the larger Z_{DR} values are due to systematic bias.

Table 4. Dataset affected by the deterioration of XPAR cross-polarization isolation.

Time (s) (2023)	Site	a	b	Max. ΔZ_{DR} across elevations before QCCPI (dB)	Max. ΔZ_{DR} across elevations after QCCPI (dB)
0614060322-064014	ZG003	0.000010	0.858	0.15	0.14
0327025411-045359	ZG060	0.001621	-2.886	0.33	0.31
0327041804-061011	ZG080	0.000985	1.040	0.24	0.23
0613165208-174725	ZG083	-0.000482	1.468	1.23	1.20

https://doi.org/10.5194/egusphere-2026-3965
Preprint. Discussion started: 28 August 2026
© Author(s) 2026. CC BY 4.0 License.

0616170340-175858	ZG100	-0.002145	-1.106	0.46	0.34
0613183159-192717	ZG101	-0.003494	-0.984	0.54	0.36
0613133704-152740	ZG100	-0.001699	-0.871	0.48	0.29
0614142623-162744	ZG020	0.002183	0.936	0.51	0.21
0614105501-125318	ZG060	-0.000482	-1.488	0.24	0.21
0614122235-141919	ZG100	-0.001941	-0.882	0.53	0.36
0616000040-020941	ZG063	-0.00114	-0.218	0.39	0.32
0617170120-190545	ZG083	-0.000701	0.978	0.53	0.49
0327031232-043732	ZG003	0.000349	0.346	0.15	0.10
0327004340-030604	ZG061	0.000432	-0.404	0.32	0.32
0327015954-041200	ZG101	0.002441	0.742	0.81	0.77

3 Experimental Results

3.1 Case Studies of Squall Lines

3.1.1 XPAR System Bias Correction

Based on the light rain observation data from the ZG100 station on June 16, 2023, as shown in Fig. 14, this study calculated the average Z_{DR} values for light rain at different elevation angles. Theoretically, under pure light rain conditions, the Z_{DR} observations from a conventional Doppler weather radar should approach 0 dB; if the actual Z_{DR} deviates significantly from 0 dB, it indicates a fixed systematic bias in the radar. Unlike conventional weather radars, the Z_{DR} observation quality of the X band phased-array weather radar is susceptible to the influence of antenna cross-polarization isolation. During the observation period from 16:06:50 to 16:36:01, according to Eq. (5), the beam pointing angle corresponding to an elevation angle of 15.3° is 0.3°, which is closest to the horizontal 0° beam state; at this time, the influence of antenna cross-polarization isolation is weakest, and the observation error is minimal. Therefore, this study selected the Z_{DR} mean value for light rain at an elevation angle of 15.3° as the reference value for correcting the Z_{DR} system bias at this station.

https://doi.org/10.5194/egusphere-2026-3965
Preprint. Discussion started: 28 August 2026
© Author(s) 2026. CC BY 4.0 License.

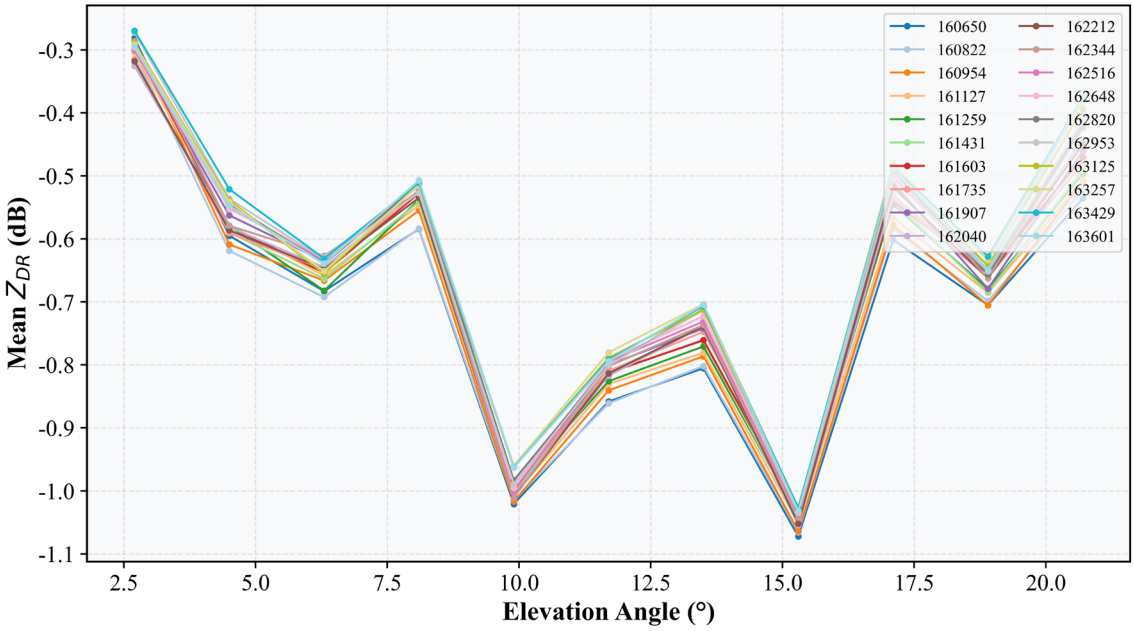

Figure 14. Average Z_{DR} values for light rain samples across different elevation angles for ZG100 XPAR, June 16, 2023, 16:06:50–16:36:01.

Time(s)	Before correction (dB)	After correction (dB)
0	0	NAN
1	29967	-0.295
2	53797	-0.548
3	62415	-0.639
4	58903	-0.507
5	57070	-0.963
6	56823	-0.794
7	54141	-0.704
8	47984	-1.042
9	41902	-0.489
10	39494	-0.649
11	37079	-0.375

https://doi.org/10.5194/egusphere-2026-3965
Preprint. Discussion started: 28 August 2026
© Author(s) 2026. CC BY 4.0 License.

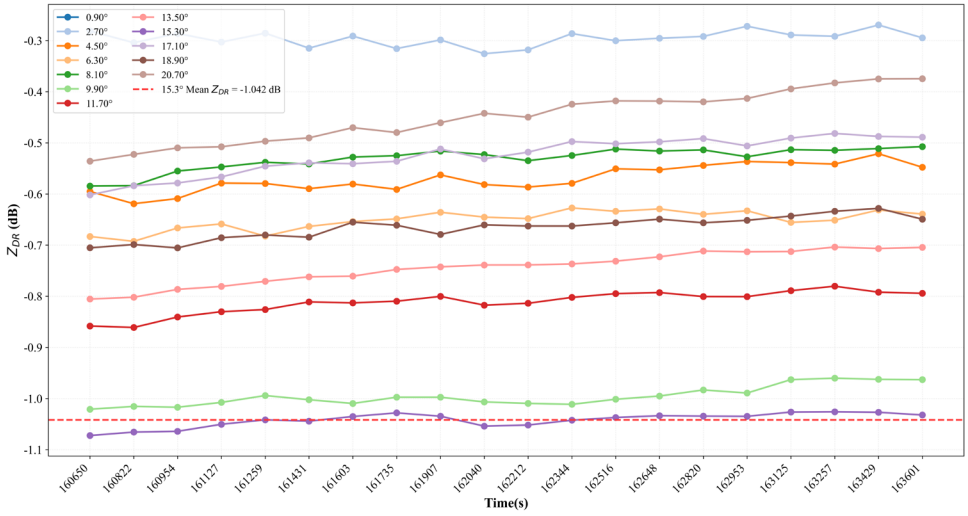

Figure 15. Time Series Plot of Z_{DR} Mean Values for Each Elevation Layer of the ZG100 Radar, June 16, 2023, 16:06:50–16:36:01.

As shown in Fig. 15, based on the light rain temporal-mean Z_{DR} plot for the ZG100 generated by XPAR, it can be observed that the mean Z_{DR} values differ for each elevation angle, but the patterns of variation are relatively stable and consistent. The mean Z_{DR} value at an elevation angle of 15.3° is -1.042 dB; this article uses this value as the system offset correction value for this site.

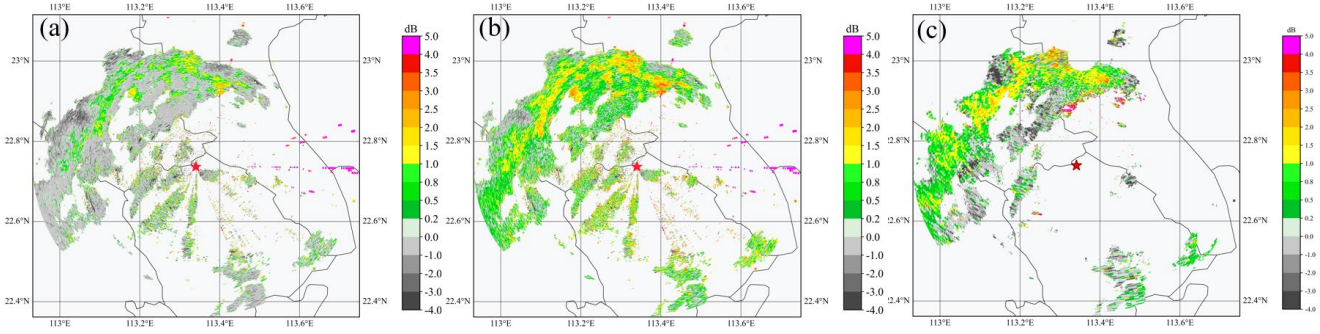

Figure 16. (a) Original XPAR Z_{DR} data. (b) XPAR data corrected for Bias-WZ$_{DR}$ method. (c) SPOL data interpolated to virtual XPAR positions.

Figure 16a shows the XPAR second-layer elevation observation results from June 6, 2023, at 01:52:49, corresponding to the core echo region of the squall line. The raw Z_{DR} data from the XPAR radar has a spatial resolution of up to 30 m × 30 m and offers excellent fine-scale detection capabilities, but it is significantly affected by system biases. Figure 16b shows the results after system bias correction. The corrected Z_{DR} data exhibits significantly improved alignment with the echo features interpolated to virtual positions by SPOL, and the distributions of the squall line core regions in both datasets are largely coincident (Fig. 16c).

https://doi.org/10.5194/egusphere-2026-3965
Preprint. Discussion started: 28 August 2026
© Author(s) 2026. CC BY 4.0 License.

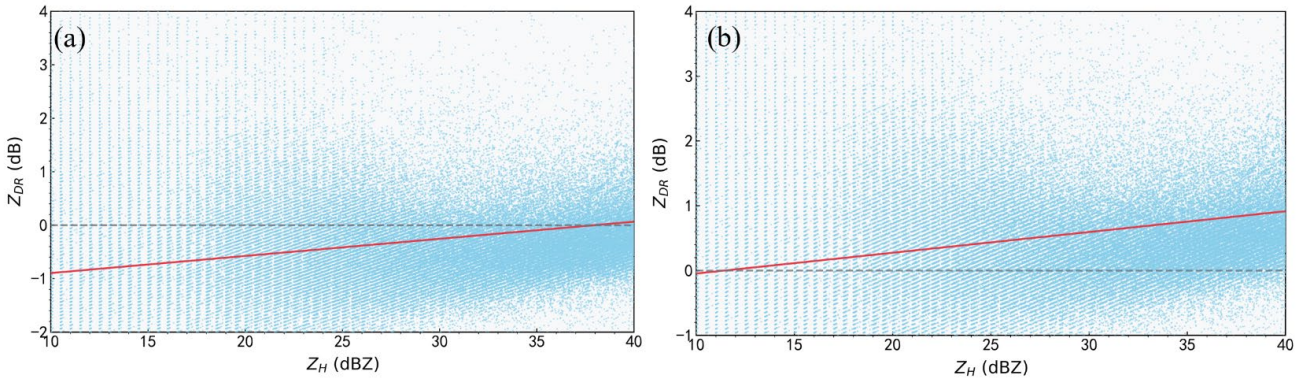

Figure 17. ZG100, June 16, 2023, 16:06:50–16:36:01, (a) $\boldsymbol{Z_{DR}}$-$\boldsymbol{Z_H}$ system before deviation correction, (b) $\boldsymbol{Z_{DR}}$-$\boldsymbol{Z_H}$ system after deviation correction.

Figure 17a shows Z_{DR} at the ZG100 site before systematic bias correction. It can be seen that Z_{DR} exhibits a significant negative systematic bias. In the scatter plot of Z_{DR} minus Z_H after correction, the values increase as raindrops grow larger; at this point, the raindrops are no longer spherical, so the values increase with raindrop size. When Z_H is between 15 and 18 dBZ, the Z_{DR} for light rain at the site is generally within 0.2 dB.

3.1.2 Correction of XPAR Cross-Polarization Isolation

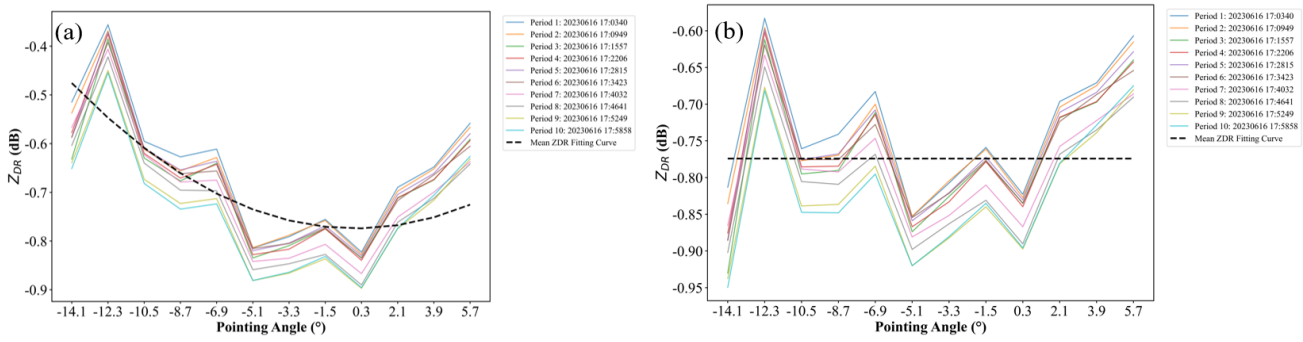

Figure 18. Z_{DR} data of ZG100 before and after QCC compensation during the period from 17:03:40 to 17:58:58 on June 16, 2023. (a) Original Z_{DR} data, degraded by cross-polarization isolation. (b) Z_{DR} data after QCCPI correction.

The degradation of cross-polarization isolation in XPAR at different beam pointing angles severely compromises the accuracy of Z_{DR} data. Since Z_{DR} plays a critical role in hydrometeor phase identification, quantitative precipitation estimation (QPE) and XPAR data quality, it is necessary to correct the Z_{DR} data of XPAR at all elevation angles using the QCC (Quadratic Curve Compensation) method. Taking data from the ZG100 site from 17:03:40 to 17:58:58 on June 16, 2023, as an example, the mean Z_{DR} values for different beam pointing angles were first calculated from 10 volume scans (each XPAR dataset having dimensions of 12 × 400 × 1400), and the results are presented in Fig. 18a.

https://doi.org/10.5194/egusphere-2026-3965
Preprint. Discussion started: 28 August 2026
© Author(s) 2026. CC BY 4.0 License.

Observations indicate that the curve exhibits a downward concave profile for beam pointing angles below 0°, whereas an upward concave profile is presented when the angle is greater than 0°. This trend is in good agreement with the quadratic curves derived from HFSS simulations. Implementation of the proposed QCC method stabilizes the maximum mean value of Z_{DR} for all elevation angles in each volume scan within 0.27 dB. Compared with the pre-correction condition (around 0.45 dB), an improvement of 0.18 dB is achieved.

When the Z_{DR} error is 0.2 dB, the error in quantitative precipitation estimation can be reduced to below 18% (Ryzhkov et al., 2005). Moreover, many scholars have indicated that a Z_{DR} error of less than 0.2 dB suggests that the radar meets the required standards for meteorological research. However, due to its high temporal and spatial resolution, phased-array radar inevitably trades off some measurement accuracy. Using the proposed method, the Z_{DR} at various pointing angles can be controlled to approximately 0.27 dB.

Table 5. The maximum difference in Z_{DR} between the off-boresight beam pointing angle and the boresight direction for ZG100.

Time(s)	Before correction (dB)	After correction (dB)
17:0340	0.47	0.27
17:0949	0.46	0.26
17:1557	0.45	0.32
17:2206	0.46	0.27
17:2815	0.46	0.29
17:3423	0.44	0.27
17:4032	0.46	0.25
17:4641	0.47	0.25
17:5249	0.45	0.26
17:5858	0.44	0.27

3.1.3 Correction Results and Analysis

This study extracted light rainfall data observed by the ZG100 XPAR radar during 16:06:50–16:36:01 on 16 June 2023 and implemented system bias correction. Subsequently, quadratic function fitting was performed on moderate rainfall data collected from 17:03:40 to 17:58:58 on the same day. On this basis, the QCC algorithm was adopted to compensate for the influence of cross isolation on the polarimetric parameter of Z_{DR}. Meanwhile, echo attenuation in moderate and heavy rainfall regions detected by the XPAR radar can be corrected by applying the attenuation correction factors computed in Eq. (2) and Eq. (3) to the original radar measurements. Figure 19 presents the three-dimensional volumetric Z_{DR} data of the ZG100 radar case (observation time: 01:35:55 on 16 June 2023), which corresponds to a typical squall line event.

Figure 19a shows the raw horizontal reflectivity Z_H from the XPAR radar, while Fig. 19b displays the Z_{DR} data of the SPOL radar interpolated to the matching spatial positions. Comparative analysis indicates that XPAR achieves favorable detection performance at low elevation angles. As a low-altitude gap-filling radar for SPOL, XPAR is characterized by higher

https://doi.org/10.5194/egusphere-2026-3965
Preprint. Discussion started: 28 August 2026
© Author(s) 2026. CC BY 4.0 License.

temporal and spatial resolution. Nevertheless, above the fourth elevation sweep, the echo intensity of XPAR decreases remarkably, accompanied by gradual degradation of echo structures.

This work mainly focuses on the correction of Z_{DR} data. Fig. 19d illustrates the results after system bias correction applied to the raw Z_{DR} (Fig. 19c). It can be seen that Z_{DR} values are close to 0 dB in light rainfall areas and range from 0 to 1 dB in moderate rainfall areas, whereas the characteristics of strong convection remain inconspicuous. Figure 19f and Fig. 19g further show the effects after additional attenuation correction and isolation bias correction, respectively. After attenuation correction, Z_{DR} values in strong convection regions increase significantly, and the retrieved squall line structure agrees better with that revealed by Z_H within the first three elevation layers (Fig. 19f). Ultimately, the comprehensively corrected results in Fig. 19g are highly consistent with the observations from the SPOL radar. Benefiting from superior temporal and spatial resolution, XPAR provides more reasonable Z_{DR} representation for squall line structures within the first four elevation layers. Restricted by the inherent detection range and receiver sensitivity of XPAR, partial loss of echo structures is observed above the fourth elevation layer. Accordingly, subsequent analyses in this study will mainly focus on the second to fourth elevation layers to elaborate on the technical advantages of the corrected XPAR products.

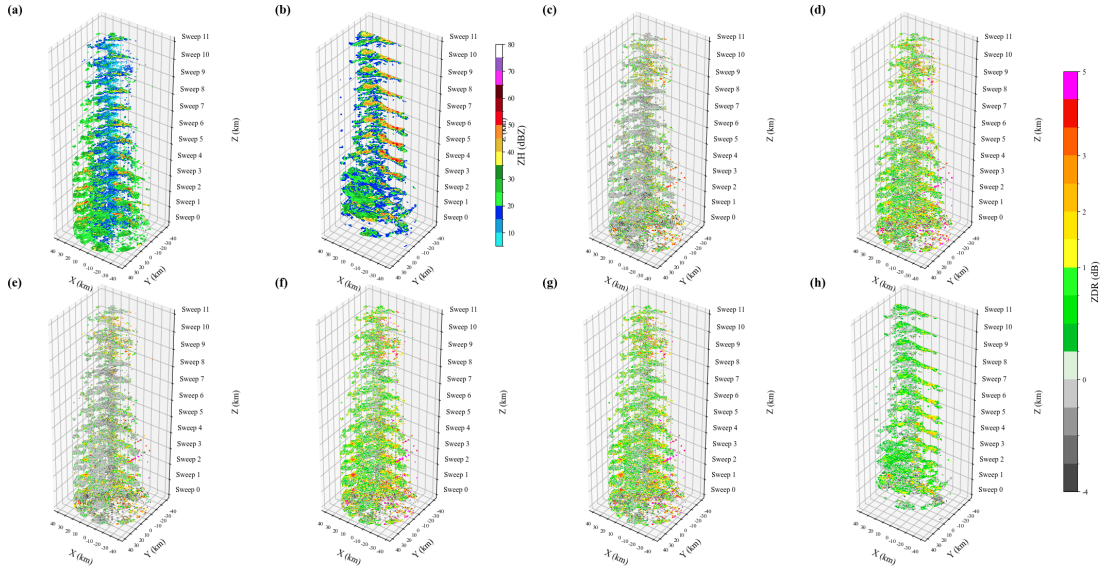

Figure 19. (a) Original Z_H of XPAR; (b) Converted Z_H of SPOL; (c) Original Z_{DR} of XPAR; (d) Z_{DR} of XPAR after Bias-WZ_{DR}; (e) Z_{DR} of XPAR after attenuation correction only; (f) Z_{DR} of XPAR after Bias-WZ_{DR} and attenuation correction; (g) Z_{DR} of XPAR after RC-Z_{DR}; (h) Converted Z_{DR} of SPOL.

https://doi.org/10.5194/egusphere-2026-3965
Preprint. Discussion started: 28 August 2026
© Author(s) 2026. CC BY 4.0 License.

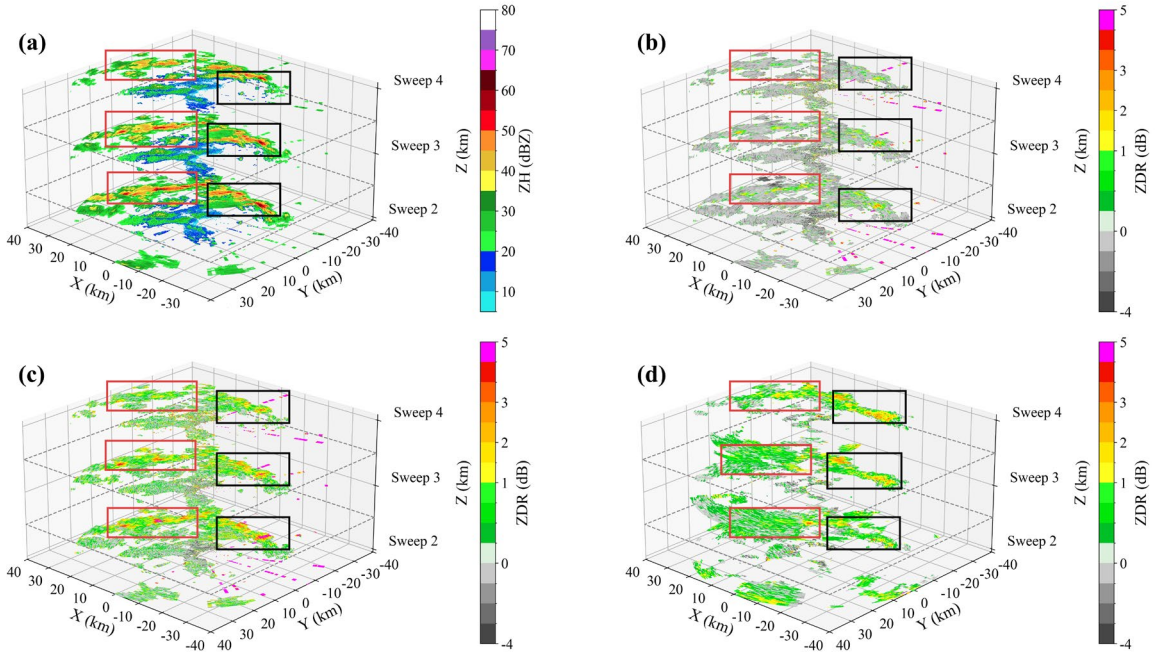

Figure 20. ZG100, squall line data at 01:35:55 on June 16, 2023. (a) Original Z_H of XPAR; (b) Original Z_{DR} of XPAR; (c) Z_{DR} of XPAR after RC-Z_{DR}; (d) Converted Z_{DR} of SPOL.

The XPAR has a detection range of 42 km, a range resolution of 30 m, and an installation height of approximately 100 m, providing high sensitivity for fine-scale observations at low elevations. During the squall line event, Z_{DR} data from the 2nd to 4th elevation sweeps were selected for comparative analysis. Figure 20 shows that the squall line exhibited a widespread banded structure. Although the raw XPAR Z_{DR} data were able to detect this squall line, a clear systematic bias was present. Figure 20d presents the Z_{DR} data of the squall line observed by the SPOL radar, interpolated onto the XPAR grid by latitude, longitude, and elevation angle. Due to the lower range resolution of SPOL compared to the higher resolution of XPAR, differences in detailed features are observed between the two radars.

As shown in Fig. 20c, which displays the XPAR Z_{DR} after RC-Z_{DR}, the Z_{DR} intensity in the squall line core region is significantly better than that in Fig. 20b, where only systematic bias correction was applied. Within the black box, the corrected XPAR Z_{DR} (Fig. 20c) and the SPOL Z_{DR} (Fig. 20d) agree well. In addition, Fig. 20c has been filtered to remove radial interference. In the red box, however, the corrected XPAR Z_{DR} data appear more physically reasonable: the banded structure is clear, with Z_{DR} exceeding 1 dB in regions where reflectivity ranges from 40 to 50 dBZ, and Z_{DR} exceeding 3 dB in localized strong convective areas where reflectivity exceeds 50 dBZ. This behavior is consistent with the actual detection characteristics of the XPAR.

https://doi.org/10.5194/egusphere-2026-3965
Preprint. Discussion started: 28 August 2026
© Author(s) 2026. CC BY 4.0 License.

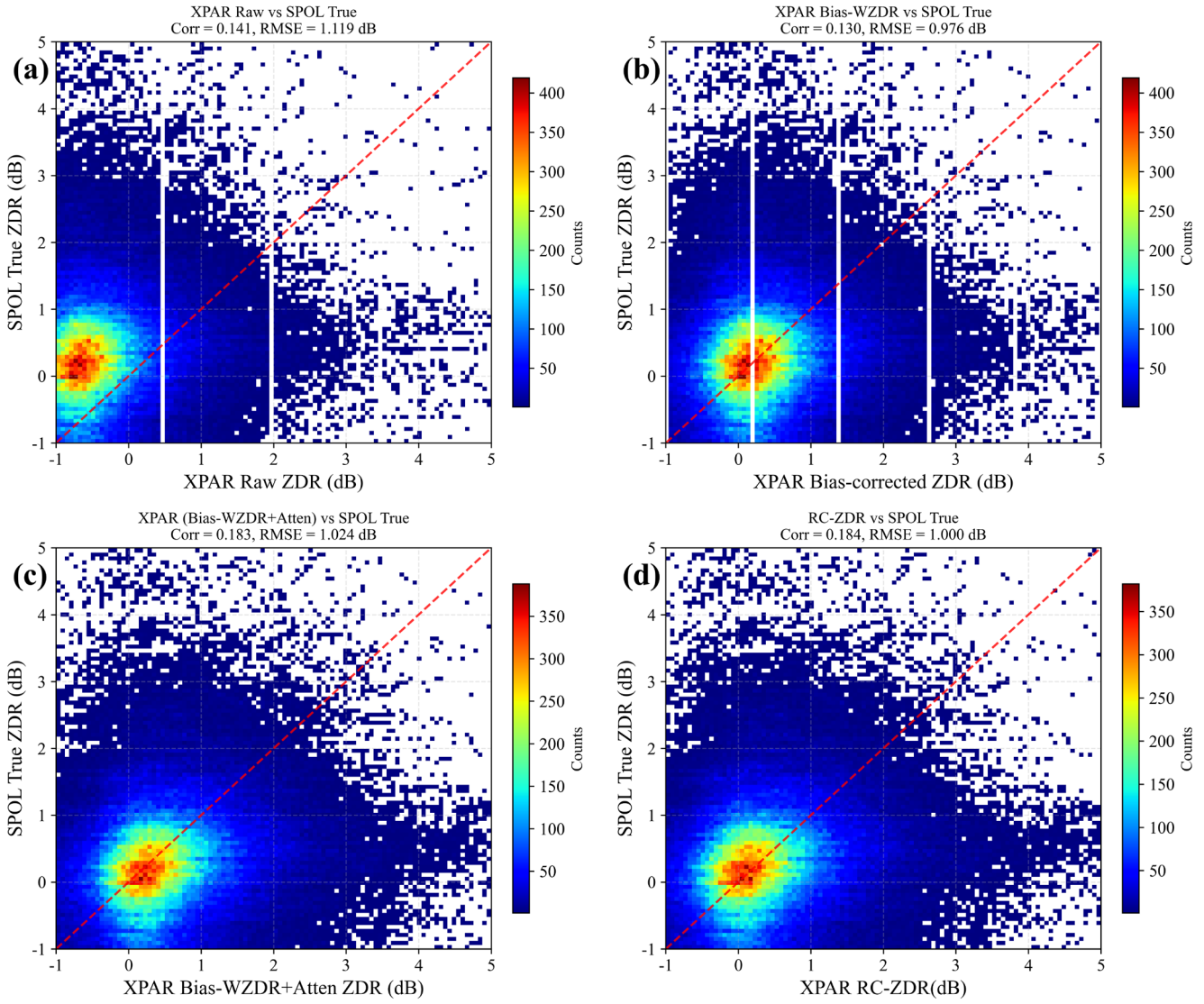

Figure 21. Comparison of XPAR and Z_{DR} data during the squall line event on June 6, 2023 (01:12:53–02:18:56). (a) Raw XPAR Z_{DR}; (b) Bias-WZ_{DR}; (c) Bias-WZ_{DR} with attenuation correction; (d) RC-Z_{DR}.

Scatter plot analysis of corrected XPAR (ZG100) data for the squall line event on June 6, 2023 (01:12:53–02:18:56) shows that: Fig. 21a presents the raw Z_{DR} data. After systematic bias correction (Fig. 21b), the data generally match the SPOL radar Z_{DR} observations. Figure 21c includes additional attenuation correction, which effectively removes the vertical white lines seen in (a) and (b) that arise from discrete missing values in the raw Z_{DR} base data. Figure 21d shows the result after further applying QCCPI isolation degradation correction. Because the QCCPI induced isolation degradation is within 0.3 dB and varies with elevation angle, its effect is not apparent in the scatter plot; however, the improvement from the isolation correction is clearly visible in Fig. 18b. In Figure 21d, the correlation coefficient (Corr) reaches 0.184 and the RMSE reaches 1.000 dB,

https://doi.org/10.5194/egusphere-2026-3965
Preprint. Discussion started: 28 August 2026
© Author(s) 2026. CC BY 4.0 License.

outperforming the original XPAR Z_{DR} data. Although Fig. 21b shows lower RMSE and Corr values, Fig. 21d corrects for the deterioration in isolation at each elevation angle in the XPAR data, resulting in smoother data across elevation angles. Table 6 presents the Z_{DR} correction results for this squall line event. After correcting for system bias, attenuation, and isolation, the original average Z_{DR} of the XPAR radar was -0.591 dB, revised to 0.328 dB, while that of the SPOL radar was 0.028 dB. The difference in Z_{DR} between XPAR and SPOL decreased from 0.619 dB to 0.3 dB. After RC-Z_{DR} correction, the average Z_{DR} of the XPAR radar was 0.226 dB, with a difference of 0.198 dB from the average Z_{DR} of the SPOL radar, remaining within 0.2 dB.

Table 6. June 6, 2023, 01:12:53–02:18:56: Comparison of Z_{DR} parameters for the ZG100 and XPAR radars at various elevation angles before and after correction.

El	XPAR-Z_{DR}	Bias-WZ_{DR}	XPAR_Bias+Att	XPAR_Bias+Att+QCCPI	RC-Z_{DR}	SPOL_Z_{DR}
El_0	-0.727	-0.747	-0.024	0.189	-0.064	0.208
El_1	-0.29	-0.305	0.523	0.719	0.499	0.045
El_2	-0.574	-0.583	0.235	0.424	0.265	0.122
El_3	-0.576	-0.587	0.242	0.394	0.284	0.100
El_4	-0.562	-0.58	0.258	0.374	0.303	0.114
El_5	-0.778	-0.791	0.027	0.106	0.068	0.034
El_6	-0.763	-0.77	0.066	0.126	0.109	-0.032
El_7	-0.693	-0.704	0.135	0.185	0.181	-0.06
El_8	-0.825	-0.84	-0.017	0.023	0.023	-0.08
El_9	-0.500	-0.534	0.308	0.345	0.338	-0.106
El_10	-0.456	-0.484	0.345	0.373	0.35	-0.12
El_11	-0.385	-0.417	0.422	0.45	0.402	-0.142
Total	-0.591	-0.607	0.209	0.328	0.226	0.028

As shown in Fig. 22, the squall line event that occurred from 01:12 to 02:36 on June 16, 2023, exhibited clear developmental characteristics: the convective system initially formed as localized severe convection and gradually organized into a linear convective band composed of a series of thunderstorm cells; By 01:30, the linear storm structure had begun to take shape, with localized Z_H exceeding 50 dBZ. The raw Z_{DR} data from the XPAR radar exhibit significant systematic bias: Z_{DR} values in areas of light and moderate rain are generally negative, while the signal in the core of the severe convection shows marked attenuation. To compare the effectiveness of radial interference filtering, this analysis retains only the raw data from the 01:24 time step as a control; radial interference filtering was applied to all other time steps (red box).

As shown in the corrected results in Fig. 23, after correction using the RC-Z_{DR} method, the quality of the XPAR Z_{DR} data in the localized severe convective core region (area marked by the blue box) has been significantly improved, accurately reflecting the characteristics of severe convective cells within the squall line structure. By 02:06, the overall intensity of the squall line had gradually weakened, and the strong echo regions had progressively evolved into a clustered distribution pattern.

https://doi.org/10.5194/egusphere-2026-3965
Preprint. Discussion started: 28 August 2026
© Author(s) 2026. CC BY 4.0 License.

Overall, compared with the SPOL radar observations, the corrected XPAR Z_{DR} data effectively characterize the convective intensity within the squall line core, and the spatial distribution characteristics of the two show better observational consistency.

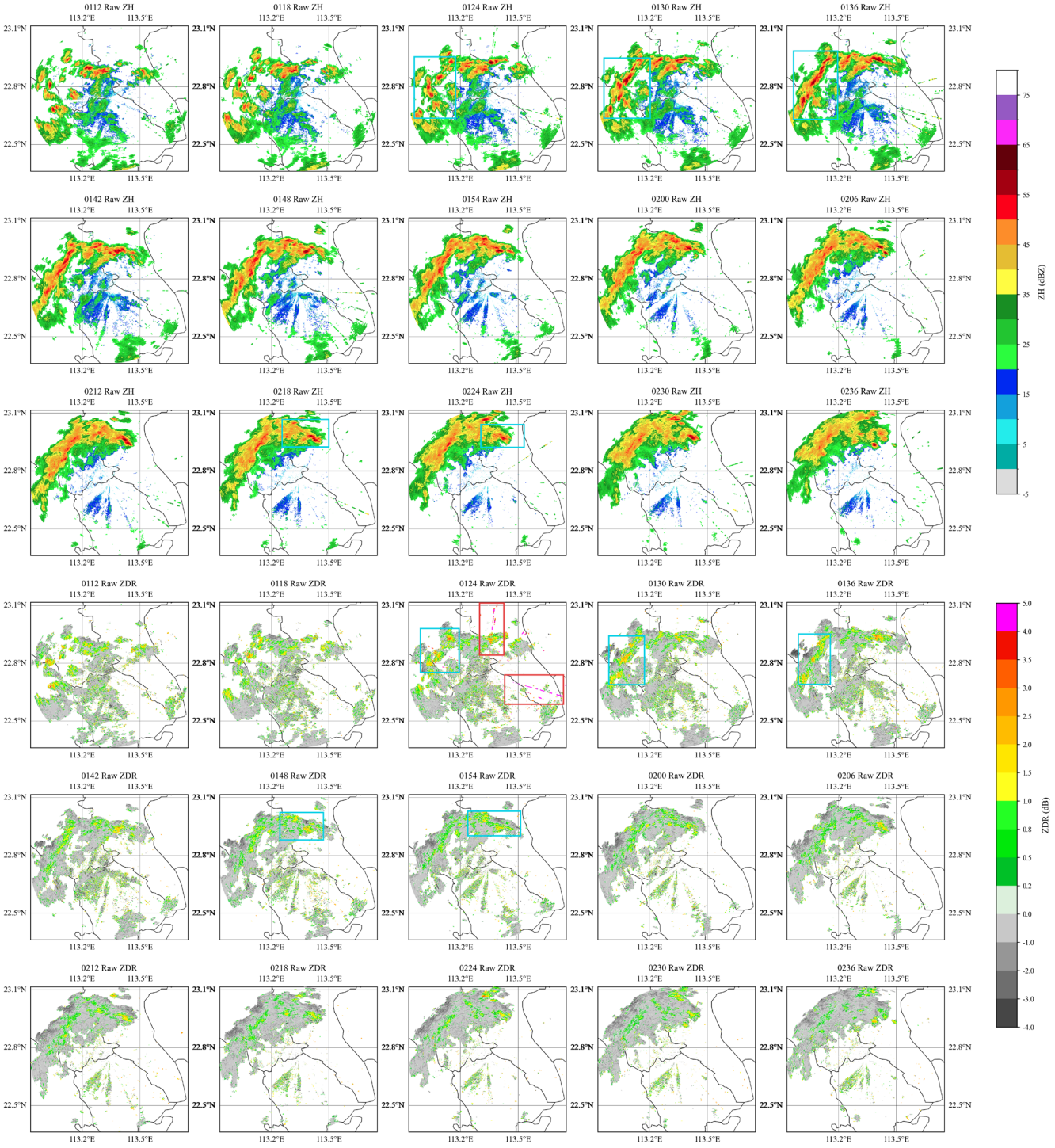

https://doi.org/10.5194/egusphere-2026-3965
Preprint. Discussion started: 28 August 2026
© Author(s) 2026. CC BY 4.0 License.

Figure 22. Lines 1-3 show the Z_H time-series observations for XPAR, while lines 4-6 show the corresponding Z_{DR} time-series observations for the same time period.

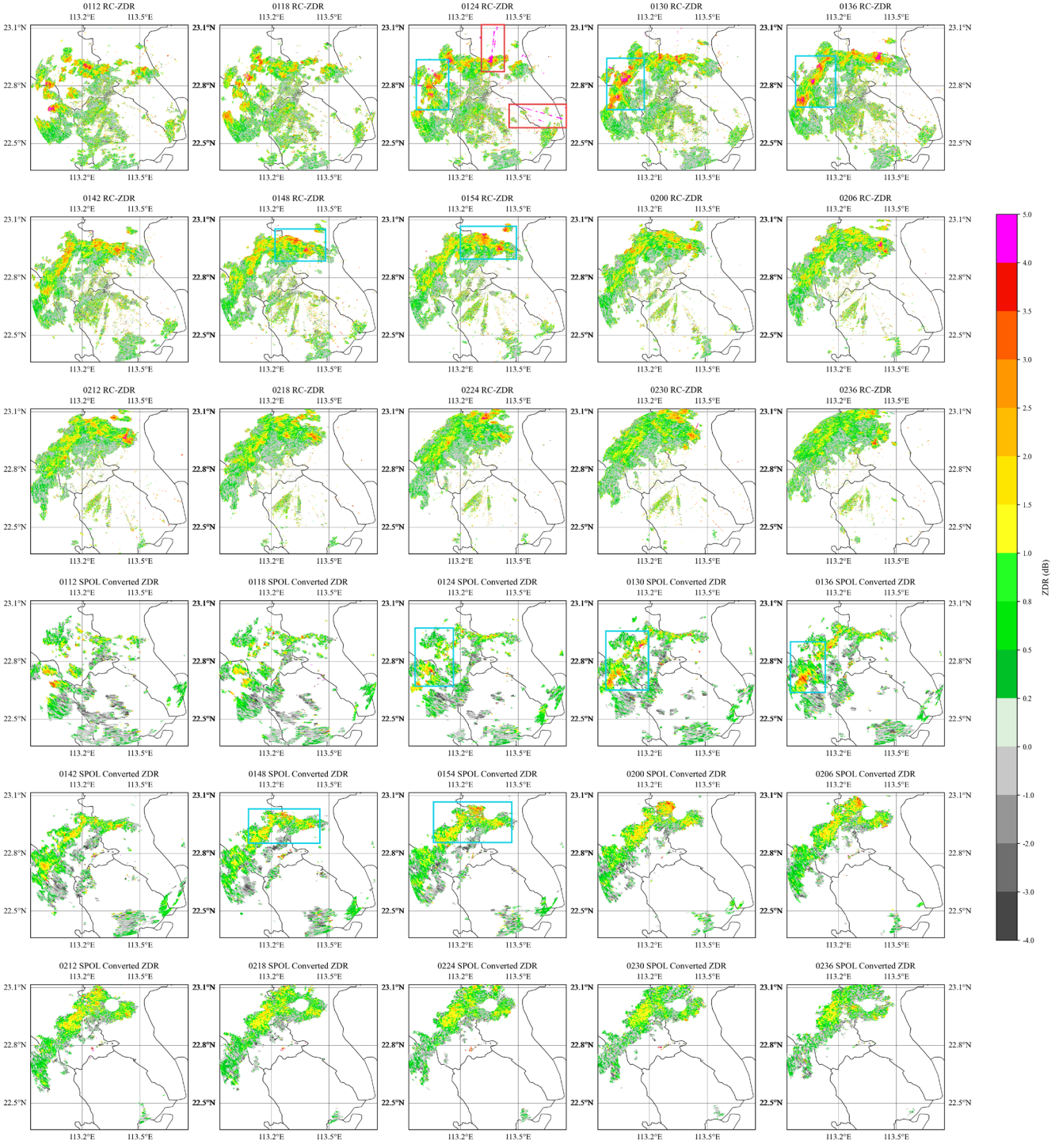

https://doi.org/10.5194/egusphere-2026-3965
Preprint. Discussion started: 28 August 2026
© Author(s) 2026. CC BY 4.0 License.

Figure 23. Lines 1-3 show the Z_{DR} time-series observations from XPAR after correction for systematic bias, attenuation, and cross-polarization isolation; lines 4-6 show the Z_{DR} time-series observations from SPOL interpolated to the same grid points for the same observation.

4 Summary and conclusions

XPAR offers high spatiotemporal resolution; however, the calibration accuracy of its Z_{DR} is constrained by multiple factors including system bias, precipitation attenuation, deterioration of cross-polarization isolation caused by beam scanning, and non-meteorological interference, making it difficult to meet the 0.2 dB accuracy requirement for operational applications. To address this issue, this paper proposes a refined Z_{DR} correction algorithm (RC-Z_{DR}) suitable for the XPAR system and validates it using observations of a squall line event at the ZG100 station, in conjunction with SPOL observations. The algorithm integrates four core correction modules: For system bias correction, the Bias-WZ_{DR} method is proposed, which uses small raindrops below the zero-degree layer as natural targets and performs a weighted average using the three elevation angles (−1.5°, 0.3°, and 2.1°) where the beam direction is closest to the array normal, thereby effectively correcting system bias; To address precipitation attenuation, corrections are applied to areas of moderate and heavy precipitation; to address the inherent deterioration of cross-polarization isolation in phased-array systems, the QCCPI method is proposed to quantitatively compensate for Z_{DR} biases caused by isolation deterioration across different elevation angles; simultaneously, a comprehensive thresholding method is employed to filter out radial interference in low-elevation observations. Validation results show that Z_{DR} observation consistency across elevation angles significantly improves after QCCPI correction alone. For the squall line event on June 6, 2023, after full RC-Z_{DR} correction, the overall mean of XPAR's Z_{DR} across all elevation angles was corrected from −0.591 dB to 0.226 dB, and the deviation relative to SPOL observations was reduced from 0.619 dB to 0.198 dB, approaching the 0.2 dB accuracy standard for meteorological research and operations. The corrected Z_{DR} data can more accurately characterize the polarization features of the severe convective core within the squall line, and the fine echo structures at low elevation angles exhibit high spatial consistency with SPOL observations. In summary, the RC-Z_{DR} algorithm proposed in this paper enables systematic correction of multiple error sources in XPAR Z_{DR} data without relying on external hardware calibration equipment. The complete correction scheme significantly improves the accuracy and stability of XPAR Z_{DR} data.

5 Outlook

Although this study achieved the expected results in correcting XPAR radar Z_{DR} data in the Guangdong region, the regional applicability of this correction algorithm still requires further validation. The current work primarily focuses on coastal plains and low-mountainous and hilly areas, whereas the topographic conditions in southwest China are extremely complex, with severe mountain occlusion posing a serious challenge to the quality of low-elevation-angle radar observations. Therefore, future research will focus on complex topographic areas in southwest China to optimize targeted correction strategies for XPAR radar Z_{DR} data. Specifically, we plan to integrate multi-source observational data from X-band radar, S-band radar, and

https://doi.org/10.5194/egusphere-2026-3965
Preprint. Discussion started: 28 August 2026
© Author(s) 2026. CC BY 4.0 License.

XPAR. Through coordinated networked observations, we aim to leverage the complementary strengths of radars operating at different frequencies and with different detection angles. This approach will enable the acquisition of high spatiotemporal resolution Z_{DR} data while effectively ensuring the inversion accuracy and spatial continuity of these parameters in complex environments. Figure 24 shows the spatial distribution of radar stations in Sichuan Province, and Figure 25 presents PPI detection results from different types of radars in 2025.

Building on the aforementioned networked observation system, the research team plans to conduct a comprehensive field experiment on weather modification in the Neijiang area of Sichuan in July 2026. The experiment will integrate various observation and operational methods, including multiple types of radar equipment, automatic surface weather stations, cloud height meters, raindrop spectrometers, ground-based high-altitude cannon systems, and unmanned aerial vehicles (UAVs), with a focus on analyzing the radiative transfer characteristics of the XPAR Z_{DR} parameters before and after artificial catalytic operations. This work will not only contribute to a deeper understanding of the mechanisms by which cloud seeding operations influence the phase state of particles within clouds and the evolution of precipitation, but will also provide robust data support and a basis for decision-making regarding the scientific evaluation of rain enhancement operations and the optimization and improvement of the technical system.

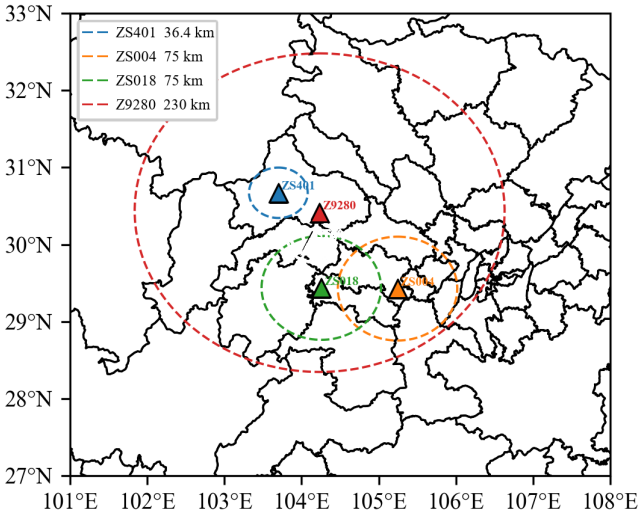

Figure 24. Distribution Map of XPAR, SPOL and XPOL in Sichuan Province. ZS401: Chongzhou X-band Phased Array Weather Radar (XPAR), ZS004: Longchang X-band Dual-Polarization Weather Radar (XPOL), ZS018: Rongxian X-band Phased Array Weather Radar (XPOL), Z9280: Longquan S-band Polarimetric Weather Radar (SPOL).

https://doi.org/10.5194/egusphere-2026-3965
Preprint. Discussion started: 28 August 2026
© Author(s) 2026. CC BY 4.0 License.

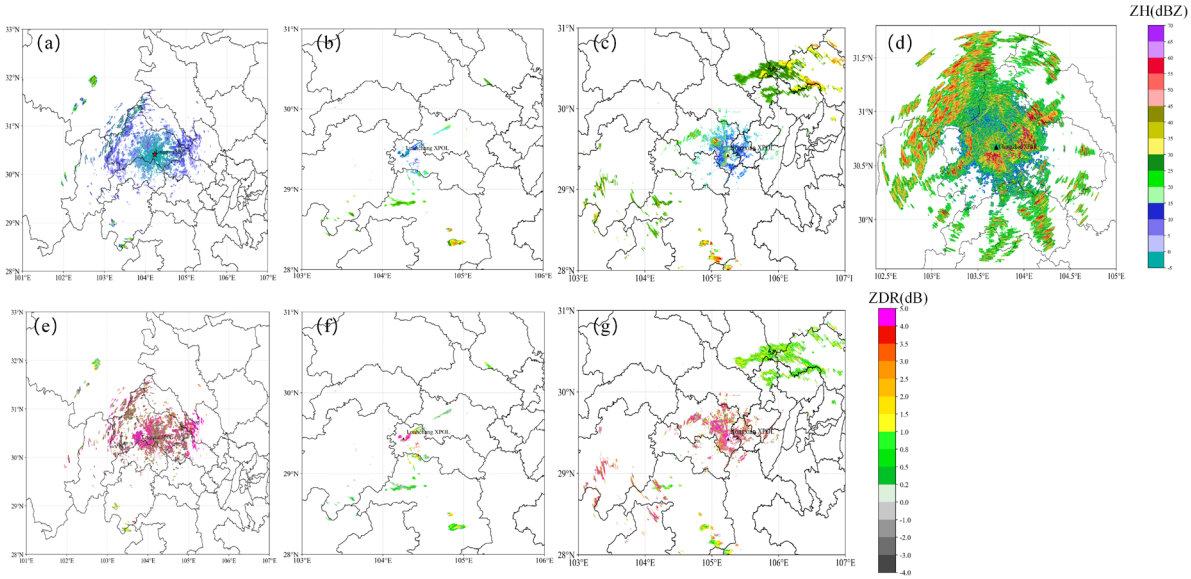

Figure 25. (a) Longquan SPOL Z_H; (b) Longchang XPOL Z_H; (c) Rongxian XPOL Z_H; (d) Chongzhou XPAR Z_H. (e) Longchang XPAR Z_{DR}. (f) Longquan XPAR Z_{DR}. (g) Rongxian XPAR Z_{DR}.

Data availability

Data are available from the authors upon request.

Author contributions

All authors contributed to the conceptualization and refinement of the study. LY did the data processing and analysis and wrote the initial draft, while JX and MX helped revise it. CW and CC collected and processed the XPAR data, JX, PW and TC performed the error calculations and analysis. JL raised professional questions and provided guidance.

Competing interests

The contact author has declared that neither they nor their co-author has any competing interests.

Disclaimer

Publisher's note: Copernicus Publications remains neutral with regard to jurisdictional claims in published maps and institutional affiliations.

https://doi.org/10.5194/egusphere-2026-3965
Preprint. Discussion started: 28 August 2026
© Author(s) 2026. CC BY 4.0 License.

Acknowledgements

This research was supported by the National Natural Science Foundation of China, Southwest China Artificial Weather Modification Capability Construction (Sichuan) Research and Experimental Project and the Guangdong Natural Science Foundation, to which we extend our sincere gratitude. We would like to thank all the authors for their collaborative efforts, as well as the reviewers for their valuable feedback.

Financial support.

This work was supported by the National Natural Science Foundation of China (U2142210), Southwest China Artificial Weather Modification Capability Construction (Sichuan) Research and Experimental Project (SCIT-ZG (Z)-2024100001), and the Natural Science Foundation of Guangdong Province (2022A1515011814).

References

Zhou, X., Yang, L., Ma, S., Wang. R., Li, Z., Song, Y., Gao, Y., and Xu, J.: Analysis of the Dynamic Process of Tornado Formation on 28 July 2024, Remote Sensing, 17,15, https://doi.org/10.3390/rs17152615, 2025.

Weber, M. E., Cho, J. Y. N., Herd, J. S., Flavin, J. M., Benner, W. E., and Torok, G. S.: The next-generation multimission US surveillance radar network, Bull. Amer. Meteor. Soc., 88, 1739–1752, https://doi.org/10.1175/BAMS-88-11-1739, 2007.

Zrnic, D. S., Kimpel, J. F., Forsyth, D. E., Shapiro, A., Crain, G., Ferek, R., Heimmer, J., Benner, W., McNellis, T. J., and Vogt, R. J.: Agile-beam phased array radar for weather observations, Bull. Amer. Meteor. Soc., 88, 1753–1766, https://doi.org/10.1175/BAMS-88-11-1753, 2007.

French, M. M., Bluestein, H. B., PopStefanija, I., Baldi, C. A., and Bluth, R. T.: Mobile, phased-array, Doppler radar observations of tornadoes at X band, Mon. Wea. Rev., 142, 1010–1036, https://doi.org/10.1175/MWR-D-13-00101.1, 2014.

Zhang, Z. and Liu, L.: Preliminary application of phased array technology in weather radar, Plat. Meteorol., 30, 1102–1107, 2011.

Liu, L., Wu, L., Wu, C., Wang, X., Chen, X., Cao, J., and Zhuang, W.: Field experiment on convective precipitation by X-band phased-array radar and preliminary results, Chin. J. Atmos. Sci., 38, 1079–1094, https://doi.org/10.3878/j.issn.1006-9895.1402.13253, 2014.

Ushio, T., Kim, D. K., Baron, P., Wada, Y., Mega, T., and Mizutani, F.: Recent progress on the phased array weather radar at X band, in: 2022 IEEE Radar Conference (RadarConf22), IEEE, 1–4, https://doi.org/10.1109/RadarConf2248738.2022.9764164, 2022.

Zhang, Y., Chen, B., Zeng, L., Shen, X., Fu, P., and Liu, X.: X-band dual-polarization phased-array radar observations of a supercell, J. Trop. Meteorol., 39, 218–229, https://doi.org/10.16032/j.issn.1004-4965.2023.021, 2023.

https://doi.org/10.5194/egusphere-2026-3965
Preprint. Discussion started: 28 August 2026
© Author(s) 2026. CC BY 4.0 License.

Palmer, R. D. and Schvartzman, D.: Emerging trends in radar: Phased arrays for weather observations, IEEE Aerosp. Electron. Syst. Mag., 40, 60–64, https://doi.org/10.1109/MAES.2024.3524937, 2025.

Zhou, X., Hu, D., Zhang, Y., I, H., and Tian, C.: Reliability of X-band dual-polarization phased array radars through comparison with an S-band dualpolarization Doppler radar, J. Trop. Meteor., 28, 218–236, https://doi.org/10.46267/j.1006-8775.2022.017, 2022.

JieLa, Q., Wang, H., Hu, S., Zhu, J., and Gao, M.: Echo simulation of dual polarization Doppler weather radar based on the physical model, EURASIP J. Wirel. Commun. Netw., 2020, 196, https://doi.org/10.1186/s13638-020-01811-4, 2020.

Bringi, V. N., Rico-Ramirez, M. A., and Thurai, M.: Rainfall estimation with an operational polarimetric C-band radar in the United Kingdom: Comparison with a gauge network and error analysis, J. Hydrometeorol., 12, 935–954, https://doi.org/10.1175/JHM-D-10-05013.1, 2011.

Cifelli, R., Chandrasekar, V., Lim, S., Kennedy, P. C., Wang, Y., and Rutledge, S. A.: A new dual-polarization radar rainfall algorithm: Application in Colorado precipitation events, J. Atmos. Ocean. Tech., 28, 352–364, https://doi.org/10.1175/2010JTECHA1488.1, 2011.

Giangrande, S. E. and Ryzhkov, A. V.: Estimation of rainfall based on the results of polarimetric echo classification, J. Appl. Meteorol., 47, 2445–2462, https://doi.org/10.1175/2008JAMC1753.1, 2008.

Palmer, R. D. and Schvartzman, D.: Emerging trends in radar: Phased arrays for weather observations, IEEE Aerosp. Electron. Syst. Mag., 40, 60–64, https://doi.org/10.1109/MAES.2024.3524937, 2025.

Li, Z., Zhang, G., and Wu, Y.: Detection and mitigation of ground clutter in polarimetric phased array radar measurements using machine learning and physics-based discriminants, IEEE Trans. Geosci. Remote Sensing, 61, 1–10, https://doi.org/10.1109/TGRS.2023.3323836, 2023.

Du, M., Liu, L., and Hu, Z.: System bias calibration of differential reflectivity for dual linear polarization radar, Plat. Meteorol., 32, 1174–1185, https://doi.org/10.7522/j.issn.1000-0534.2012.00084, 2013.

Matsuda, K. and Onishi, R.: Turbulent enhancement of radar reflectivity factor for polydisperse cloud droplets, Atmos. Chem. Phys., 19, 1785–1799, https://doi.org/10.5194/acp-19-1785-2019, 2019.

Bringi, V. N., Chandrasekar, V., Balakrishnan, N., and Zrnic, D. S.: An examination of propagation effects in rainfall on radar measurements at microwave frequencies, J. Atmos. Ocean. Tech., 7, 829–840, https://doi.org/10.1175/1520-0426(1990)007<0829:AEOPEI>2.0.CO;2, 1990.

Burgemeister, F., Clemens, M., and Ament, F.: Reanalysis of multi-year high-resolution X-band weather radar observations in Hamburg, Earth Syst. Sci. Data, 16, 2317–2332, https://doi.org/10.5194/essd-16-2317-2024, 2024.

Jha, A. K., Bhat, G. S., Kalapureddy, M. C. R., and Pandithurai, G.: Bias correction of an X-band radar reflectivity data to improve spatial rainfall estimation, J. Earth Syst. Sci., 133, 59, https://doi.org/10.1007/s12040-024-02271-w, 2024.

Ryzhkov, A. V., Giangrande, S. E., Melnikov, V. M., and Schuur, T. J.: Calibration issues of dual-polarization radar measurements, J. Atmos. Ocean. Tech., 22, 1138–1155, https://doi.org/10.1175/JTECH1772.1, 2005.

https://doi.org/10.5194/egusphere-2026-3965
Preprint. Discussion started: 28 August 2026
© Author(s) 2026. CC BY 4.0 License.

Williams, E., Hood, K. T., Cho, J. Y. N., Smalley, D. J., Sandifer, J. B., Zrnic, D., Melnikov, V. M., Burgess, D. W., Forsyth, D., Webster, T. M., and Erickson, D.: End-to-end calibration of NEXRAD differential reflectivity with metal spheres, in: Proc. 36th Conf. Radar Meteorol., 9, 2013.

Yin, J., Hoogeboom, P., Unal, C., Russchenberg, H., van der Zwan, F., and Oudejans, E.: UAV-aided weather radar calibration, IEEE Trans. Geosci. Remote Sensing, 57, 10362–10375, https://doi.org/10.1109/TGRS.2019.2933912, 2019.

Sanchez-Rivas, D. and Rico-Ramirez, M. A.: Calibration of radar differential reflectivity using quasi-vertical profiles, Atmos. Meas. Tech., 15, 503–520, https://doi.org/10.5194/amt-15-503-2022, 2022.

Frech, M. and Hubbert, J.: Monitoring the differential reflectivity and receiver calibration of the German polarimetric weather radar network, Atmos. Meas. Tech., 13, 1051–1069, https://doi.org/10.5194/amt-13-1051-2020, 2020.

Zhu, J., Liu, L., Wu, C., Zhou, Q., Liu, Y., Gao, S., Geng, F., and Huang, H.: Observational deviation and correction caused by multi-beam scanning mode from X-band phased array weather radar, J. Trop. Meteorol., 41, 647–660, https://doi.org/10.16032/j.issn.1004-4965.2025.055, 2025.

Zhang, G., Doviak, R. J., Zrnic, D. S., Crain, J., Staiman, D., and Al-Rashid, Y.: Phased array radar polarimetry for weather sensing: a theoretical formulation for bias corrections, IEEE Trans. Geosci. Remote Sensing, 47, 3679–3689, https://doi.org/10.1109/TGRS.2009.2029332, 2009.

Heberling, W. and Frasier, S. J.: On the projection of polarimetric variables observed by a planar phased-array radar at X-band, IEEE Trans. Geosci. Remote Sensing, 59, 3891–3903, https://doi.org/10.1109/TGRS.2020.3023640, 2020.

Heberling, W. and Frasier, S. J.: Evaluation of phased-array weather-radar polarimetry at X-band, in: 2018 IEEE Radar Conference (RadarConf18), IEEE, 0851–0855, https://doi.org/10.1109/RADAR.2018.8378671, 2018.

Zhang, W., Wu, C., Liu, L., Zhang, Y., Bao, X., and Huang, H.: Research on quantitative comparison and observation precision of dual polarization phased array radar and operational radar, Plat. Meteorol., 40, 424–435, https://doi.org/10.7522/j.issn.1000-0534.2020.00056, 2021.

Ho, J., Li, Z., and Zhang, G.: Quantitative error analysis of polarimetric phased-array radar weather measurements to reveal radar performance and configuration potential, Atmos. Meas. Tech., 18, 619–638, https://doi.org/10.5194/amt-18-619-2025, 2025.

Zrnic, D. S., Zhang, G., and Doviak, R. J.: Bias correction and Doppler measurement for polarimetric phasedarray radar, IEEE Trans. Geosci. Remote Sensing, 49, 843–853, https://doi.org/10.1109/TGRS.2010.2057436, 2011.

Zhang, G.: Weather Radar Polarimetry, CRC Press, Boca Raton, FL, 304 pp., ISBN 1439869588, 2016.

Dorsey, W. M., Scholnik, D. P., and Stumme, A.: Performance comparison of planar, cylindrical, and polygonalized phased arrays for surveillance and ubiquitous radar, IEEE Trans. Aerosp. Electron. Syst., 58, 596–602, https://doi.org/10.1109/TAES.2021.3111789, 2022.

Fulton, C., Kenworthy, P., Lujan, J., Herndon, M., Garner, S., and Thompson, D.: Mutual coupling-based calibration for the Horus Digital Phased Array Radar, in: 2022 IEEE International Symposium on Phased Array Systems & Technology (PAST), Waltham, MA, USA, 11–14 October 2022, IEEE, https://doi.org/10.1109/past49659.2022.9974962, 2022.

https://doi.org/10.5194/egusphere-2026-3965
Preprint. Discussion started: 28 August 2026
© Author(s) 2026. CC BY 4.0 License.

Ivic, I. R.: Cross-coupling mitigation in polarimetric par via antenna tilt, J. Atmos. Ocean. Tech., 40, 587–604, https://doi.org/10.1175/jtech-d-22-0059.1, 2023.

Zhang, G., Doviak, R. J., Zrnic, D. S., Crain, J., Staiman, D., and Al-Rashid, Y.: Phased array radar polarimetry for weather sensing: A theoretical formulation for bias corrections, IEEE Trans. Geosci. Remote Sensing, 47, 3679–3689, https://doi.org/10.1109/TGRS.2009.2029332, 2009.

He, Y., Zhang, T., He, H., Yin, J., and Yang, J.: A system optimization scheme for bias correction of polarimetric phased-array radar, IEEE Trans. Geosci. Remote Sensing, 61, 1–17, https://doi.org/10.1109/TGRS.2023.3237841, 2023.

Diong, J.-Y., Xavier, P., Abdullah, M. F. A., and Schwendike, J.: The characteristics of squall lines in the Southeast Asia region, Q. J. Roy. Meteor. Soc., e70143, https://doi.org/10.1002/qj.70143, 2026.

Lopez-Bravo, C., Vincent, C. L., Huang, Y., and Lane, T. P.: A case study of a West Sumatra squall line using satellite observations, Mon. Weather Rev., 151, 523–543, https://doi.org/10.1175/MWR-D-21-0194.1, 2023.

Chen, Z., Zhao, P., Xiao, H., Zhao, C., and Li, H.: Lane effect of cloud microphysical processes on surface wind of a squall line in South China, Atmos. Res., 315, 107828, https://doi.org/10.1016/j.atmosres.2024.107828, 2025.

Swastiko, W. A., Tsai, C.-L., Kim, S. H., and Lee, G.: Kinematic and dynamic structure of the 18 May 2020 squall line over South Korea, Remote Sens., 16, 1474, https://doi.org/10.3390/rs16081474, 2024.

Zhou, X., Hu, D., Zhang, Y., Li, H., and Tian, C.: Reliability of X-band dual-polarization phased array radars through comparison with an S-band dual-polarization Doppler radar, J. Trop. Meteorol., 28, 2, https://doi.org/10.46267/j.1006-8775.2022.017, 2022.

Wen, H., Wang, H., Zhang, Y., Wu, L., and Li, R.: Analysis and correction of system bias of differential reflectivity for X-band dual polarization radars in Beijing area, Plat. Meteorol., 44, 393–406, https://doi.org/10.7522/j.issn.1000-0534.2024.00073, 2025.

Wang, L., Wang, Y., Liu, M., Chen, W., and Li, C.: Analysis of dual-polarimetric radar observations of precipitation phase during snowstorm events in Jiangsu Province, China, Atmosphere, 15, 321, https://doi.org/10.3390/atmos15030321, 2024.

Fišer, O. and Kovalchuk, M.: On theoretical accuracy of meteorological targets measurement by radar, Radioengineering, 31, 176–184, https://doi.org/10.13164/re.2022.0176, 2022.

Zhang, Z.: Evaluation of echo intensity of phased array weather radar, Ph.D. thesis, Chinese Academy of Meteorological Sciences, Beijing, China, 2011.

An, W., Tian, X., Wang, J., and Wang, S.: Low-profile dual-polarized double-layer microstrip antenna for 5G and 5G Wi-Fi, Micromachines, 14, 942, https://doi.org/10.3390/mi14050942, 2023.

Ryzhkov, A. V., Giangrande, S. E., Melnikov, V. M., and Schuur, T. J.: Calibration issues of dual-polarization radar measurements, J. Atmos. Ocean. Technol., 22, 1138–1155, https://doi.org/10.1175/JTECH1772.1, 2005.

https://doi.org/10.5194/egusphere-2026-3965
Preprint. Discussion started: 28 August 2026
© Author(s) 2026. CC BY 4.0 License.

Park, S. G., Bringi, V. N., Chandrasekar, V., Maki, M., and Iwanami, K.: Correction of radar reflectivity and differential reflectivity for rain attenuation at X band. Part I: Theoretical and empirical basis, J. Atmos. Ocean. Tech., 22, 1621–1632, https://doi.org/10.1175/JTECH1803.1, 2005.

An, W., Tian, X., Wang, J., and Wang, S.: Low-profile dual-polarized double-layer microstrip antenna for 5G and 5G Wi-Fi, Micromachines, 14, 942, https://doi.org/10.3390/mi14050942, 2023.